



저작자표시-비영리-변경금지 2.0 대한민국

이용자는 아래의 조건을 따르는 경우에 한하여 자유롭게

- 이 저작물을 복제, 배포, 전송, 전시, 공연 및 방송할 수 있습니다.

다음과 같은 조건을 따라야 합니다:



저작자표시. 귀하는 원저작자를 표시하여야 합니다.



비영리. 귀하는 이 저작물을 영리 목적으로 이용할 수 없습니다.



변경금지. 귀하는 이 저작물을 개작, 변형 또는 가공할 수 없습니다.

- 귀하는, 이 저작물의 재이용이나 배포의 경우, 이 저작물에 적용된 이용허락조건을 명확하게 나타내어야 합니다.
- 저작권자로부터 별도의 허가를 받으면 이러한 조건들은 적용되지 않습니다.

저작권법에 따른 이용자의 권리는 위의 내용에 의하여 영향을 받지 않습니다.

이것은 [이용허락규약\(Legal Code\)](#)을 이해하기 쉽게 요약한 것입니다.

[Disclaimer](#)

공학박사 학위논문

심폐질환의 질병특성 분석을 위한
의료영상에서의 물리적 운동 계량

Assessment of physical motions on medical images
for cardiac and pulmonary diseases analysis

울산대학교 대학원

의 학 과

최 승 현

심폐질환의 질병특성 분석을 위한
의료영상에서의 물리적 운동 계량

지도교수 김 남 국

이 논문을 공학박사 학위 논문으로 제출함

2020년 8월

울산대학교대학원

의 학 과

최 승 현

최승현의 공학박사 학위 논문을 인준함

심사위원 하 호 진 (인)

심사위원 이 호 연 (인)

심사위원 오 연 목 (인)

심사위원 서 준 범 (인)

심사위원 김 남 국 (인)

울 산 대 학 교 대 학 원

2020 년 8 월

Abstract

In the progression of cardiac & pulmonary diseases, morphological and physical characteristics change. Though heart and lung require physical motions to maintain vital activities, there is a knowledge gap between physical characteristics and pathophysiological aspects of the cardiac and pulmonary diseases. To fill the gap, image registration based physical motion analysis methods were constituted and assessed through several applications, such as Chronic Obstructive Pulmonary Disease (COPD), Idiopathic Pulmonary Fibrosis (IPF), drug-induced cardiomyopathies.

The constituted framework for the motion of biomechanical media provides fully 12 degrees of freedom as two subgroups; displacement and deformation, of which comparison is essential to understand the behavior of the target media as the results of the load – resistance competitions. More specifically, 2 types of directional information about motion were derived in every point-grid in the domain of calculation: directions of motion and loaded face.

Firstly, two or more volume images at specific dynamic phases of motion were registered by using the series of rigid, non-rigid, and level-set registration techniques to calculate displacement fields at every measured point within the target domain. Then the calculation of deformation fields was constituted using the concept of continuum in applied physics, which provides theoretical frameworks for the physical motions of continuous media with finite volume, i.e., solids or fluids. Measures representing different aspects of biomechanical motion were derived from the calculated deformation fields and applied to the COPD, IPF, drug-induced cardiomyopathies.

In conclusion, theoretical and technical frameworks providing the physical motion in medical images were constituted with the image registration, and measures representing the physical motions are expected to have the potential usefulness in understanding the physiological status of cardiac and pulmonary diseases.

Contents

Abstract	i
Contents	ii
List of Tables.....	v
List of Figures	vi
1. Introduction	1
1.1. Pulmonary & Cardiac Diseases	1
1-2. Physiology relating Function to Physics.....	2
1-2-1. Former researches	3
1-2-1-1. Needs for physical analysis.....	3
1-3. Outlines	5
2. Methods.....	6
2-1. Image Registration	6
2-1-1. Preprocessing.....	8
2-1-2. Cost functions (Similarity measures).....	10
2-1-3. Optimization	10
2-1-4. Transformation.....	11
2-1-5. Interpolation.....	13
2-2. The physical motion of a body	14
2-2-1. Concept of continuum media.....	14
2-2-2. Deformation vs displacement	15
2-2-3. Generalized expression of motion	18
2-2-4. Strain tensor as a deformation	21
2-2-4-1. Lagrangian strain tensor.....	21
2-2-4-2. Infinitesimal versus finite strain.....	23
2-3. Assessment of physical motion	24
2-3-1. Volumetric changes	24

2-3-2. Principal strain	27
2-3-3. Equivalent strain	28
2-4. Sources of bias	30
2-4-1. Bias in registration	30
2-4-2. Bias from mode and scale of motion	31
2-4-3. Smoothing	33
2-4-4. Bias scales in each calculation steps	34
2-5. Contribution and Implication	38
2-5-1. Pixel-wise motion in full (12) degree of freedom	38
2-5-2. Physical regime for ‘large’ deformation.....	38
2-5-3. Clinical implication on each degree of motion.....	38
3. Application to diseases	46
3-1. Chronic Obstructive Pulmonary Disease (COPD)	46
3-1-1. Materials	48
3-1-1-1. Subject and Dataset – KOLD Cohort	48
3-1-1-2. Image-based physical Biomarkers	50
3-1-1-3. Clinical Measures	51
3-1-2. Results & Discussions.....	53
3-1-2-1. Correlation with Clinical Measures	55
3-1-2-2. Mortality & Acute Exacerbation	59
3-1-2-3. Prognosis in 6 years.....	60
3-2. Idiopathic Pulmonary Fibrosis	63
3-2-1. Materials	64
3-2-1-1. Subjects and Dataset	64
3-2-1-2. Image-based physical Biomarkers	65
3-2-1-3. Clinical Measures	65
3-2-2. Results & Discussions.....	66
3-3. Left Ventricle Contractility.....	67
3-3-1. Materials & Methods	68

3-3-1-1. Subjects and Dataset	68
3-3-1-2. Image-based physical Biomarkers	68
3-3-1-3. Clinical Measures	71
3-3-2. Results & Discussions	71
4. Implications from three applications.....	77
5. Conclusion	79
6. References	80

List of Tables

Table 1. Mutual information calculated from the registration of randomly selected 1 one 6 portions of study cases for COPD and IPF.....	34
Table 2. Categories of strain analysis; vector-based (direction) vs scalar-based (regime)	42
Table 3. Baseline and 3rd-year follow-up characteristics of 60 COPD patients.....	49
Table 4. Physical biomarkers in baseline and 3rd year follow-up of 60 COPD patients	55
Table 5. Associations by Spearman’s correlation coefficients (ρ) between physical biomarkers (AAVC%, EVM, Emphysema Index%) in baseline and clinical measures (6MWD, SGRQ score, FEV1%, cDLCO%, BMI, Dyspnea scale)	56
Table 6. Associations by Spearman’s correlation coefficients (ρ) between physical biomarkers (AAVC%, EVM, Emphysema Index%) in baseline and clinical measures (6MWD, SGRQ score, FEV1%, cDLCO%, BMI, Dyspnea scale) in 3rd year follow-up.	57
Table 7. Associations by Spearman’s correlation coefficients (ρ) between physical biomarkers (AAVC%, EVM, Emphysema Index%) in baseline and three-year changes in clinical measures (Δ 6MWD, Δ SGRQ score, Δ FEV1%, Δ cDLCO%, Δ BMI, Δ Dyspnea scale).	57
Table 8. Parameters estimated by a multivariable linear regression model for Δ FEV1% as dependent variable and AAVC%, EVM, Emphysema Index%, Pack-year, age, BMI, Dyspnea scale, 6-minute walk distance, and SGRQ score as independent variables.....	58
Table 9. Association between AAVC%, EVM and 6-year prognosis of FEV1%, 6MWD, and dyspnea scale.	60
Table 10. Demographics of 30 IPF Patients	64
Table 11. Associations by Pearson’s correlation coefficients between 5 stratifies AAVC in HAA, and FVC%.....	66
Table 12. Associations by Pearson’s correlation on the three-dimensional echocardiographic global strains and left ventricular systolic functions measured by catheterization.....	72
Table 13. Association by Pearson’s correlation on the left ventricular systolic functions measured by catheterization and three-dimensional global strains corrected by residual volume ratio.....	73

List of Figures

Figure 1. Analyzing the physical aspects of the disease-induced remodeling of the lung will fill the gap between cellular, microscopic, and macroscopic functional understanding of the disease.	2
Figure 2. Framework for the image to image registration (example images: Lung CT).....	6
Figure 3. Example of image segmentation	8
Figure 4. Concept of normalization in CT images.....	9
Figure 5. Descriptions on the physical motion of the material body, which can be decomposed into displacement and deformation.	15
Figure 6. Example of the inhomogeneity in material properties; from the motion analysis by comparing the deformation and displacement	16
Figure 7. Physical body's configuration change (from undeformed to deformed, including rigid body motions) designed to separate deformation from the generalized motion	18
Figure 8. Types of the deformation in stain tensor, defined by the combination of the two directional basis	22
Figure 9. Physical body's configuration change (from undeformed to deformed, including rigid body motions) designed to separate deformation from the generalized motion.	31
Figure 10. Example of smoothing on volumetric deformation (AAVC%) during inspiration; lung CT image at inspiration; (a) raw medical image, (b) unsmoothed volumetric deformation, (c) smoothed volumetric deformation by gaussian filter with 3-pixel depth. ...	33
Figure 11. Schematic diagram showing the role of mechanical stress-induced lung remodeling (modified, figure 1 of literature ¹⁴)	40
Figure 12. (a) The direction of the principal strain calculated in the normal beagle with the speckle tracking point-grid from echocardiology, representing the contractile motion of myocardial fibers, (b) the helical anatomy and biomechanical direction of motion ⁵⁰	44
Figure 13. Emphysematous area (arrow-line) in inspiratory(a), and expiratory(b) CT Image of severe COPD patient (FEV1% =24%).....	46
Figure 14. Survival curves for high- and low- strata stratified by (a) AAVC% and (b) EVM. 95% confidence interval is shown in shades.	59

Figure 15. Exacerbation-free survival curves for high- and low- strata stratified by (a) AAVC%, and (b) EVM. 95% confidence interval is shown in shades.....	60
Figure 16. UIP patterns (arrow-line) in inspiratory CT Image of IPF patient (FVC% =41%)	63
Figure 17. AAVC% of whole lung and HAA augmented AAVC% over -600, -700, -800, -900 in (HU), during expiration.....	65
Figure 18. Generation of triangular mesh. In each time frame, grids of speckle-tracking points were obtained at the LV endocardial surface to analyze temporal motion of a curved surface in three-dimensional space.	69
Figure 19. Principal analysis where in the concurrent coordinate having no shear deformations.....	70
Figure 20. Three-dimensional principal strain line patterns of the left ventricular endocardium; (a) Representative vector map of principal strains at mid-systole. (b,c) Time evolution of the global strains obtained from 14 dogs at the baseline state: (b) principal (GP1S) and secondary (GP2S) strains, and (c) longitudinal (GLS) and circumferential (GCS) strains. The values are presented as mean \pm standard deviation using error bars.	72

1. Introduction

1.1. Pulmonary & Cardiac Diseases

(Motivation on researching the physical status of lung and heart) Half of the top 10 global causes of deaths are cardiac and pulmonary diseases ¹. Moreover, both organs are required to persist cyclic motions in lifetimes to sustain its function, providing air and blood flows in the body. Thus, the dynamic status – physical motion – of the heart and lung can be one of the closest clues and cumulative results of the pulmonary and cardiac diseases.

One major way of non-invasive observation on physical status is imaging. In the early stage of the digitalized medical imaging technique, cardiac and pulmonary motions are the source of the artifacts, deprecating the image quality ²⁻⁴. However, as the imaging technology progresses, three dimensional and/or real-time imaging is spreading widely to the clinical care of cardiac and pulmonary diseases ⁵⁻⁸. Accordingly, researchers investigated various categories of imaging biomarkers, and the predominant portion of biomarkers are direct thresholding, calculus, and combinations of imaging intensity ⁹⁻¹².

1-2. Physiology relating Function to Physics

Physiological understanding of a specific disease normally starts from the academic domains studying microscale mechanism as cell biology or immunology, as pathological remodeling of the tissues or cells is taking place on a spectrum between (i) microscopic scale composed of various cells, extracellular matrix molecules, and signaling substances that make up differentiated functional micro-units, and (ii) macroscopic scale covering the entire organ and the body. Under the paradigm of reductionism, many studies of cell biology, physiology, and biochemistry have been conducted to reveal the microscopic behavior of each component; however, heart and lung are a holistic system in which heterogeneous physiological and physical effects in microscale interact to provide behavior in a macro scale.

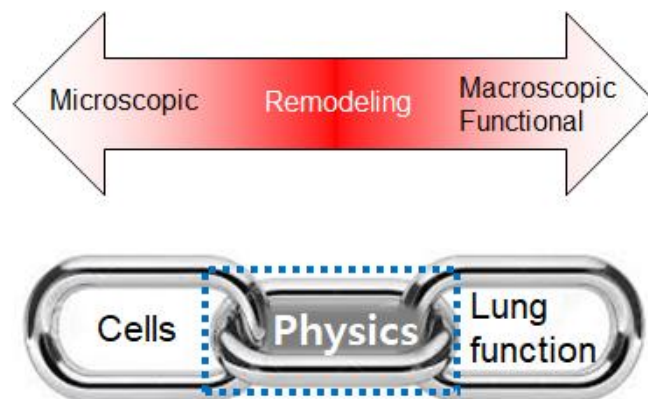


Figure 1. Analyzing the physical aspects of the disease-induced remodeling of the lung will fill the gap between cellular, microscopic, and macroscopic functional understanding of the disease.

Applied physics provides viewpoints to find out how the microscopic components lead to changes in collective behavior and provides means to quantify how these collective behaviors translates to the functional changes. Thus, combined application to the cardiac and pulmonary organ would fill the missing link between the ends of the scale spectrum.

1-2-1. Former researches

1-2-1-1. Needs for physical analysis

As an example, for the need for physical analysis in the lung, out of the three applications cases of former researches about COPD is described below.

Eye-opening progress are made in research from cell biology or physiological point of view in exploring the mechanism of lung parenchymal damage, which is the core of the pathophysiology of COPD.

The lung parenchyma is a complex of numerous types of cells and tissues, such as endothelium, epithelium, fibroblasts, secretory cells, interstitial stem cells, immune cells, and extracellular matrix those conform the gas-exchange apparatus including alveoli, airways, and microvascular system. The cells and extracellular matrix that make up the lung have their own designated turn-over cycle consisted of growth-destruction-death-regeneration, in response to immune responses to extrinsic irritants or oxidative stress.

These process keeps the gas-exchange surface intact to keep the lung functional. The cellular and molecular aspects of the lung maintenance system are revealed in detail ¹³. Epithelial cells under stress secret inflammation signal and initiates apoptosis. The inflammation signal recruits macrophage to clean up the damaged cells by phagocytosis and activates proteinase to digest the extracellular matrix. And then, fibroblasts and stem cells are recruited to regenerate the deleted parenchyma.

However, repeated stress could disrupt the normal regeneration process leaving irreversible damage to the lung parenchyma ¹⁴. The extracellular matrix is composed of fibrous proteins such as collagen, elastin, and peptidoglycans. Repeated mechanical stress over time breaks the fibrous network leading to reduced elastic recoil. The mechano-transduction pathway is revealed in quite a detail ¹⁵, but the understanding are mostly on the cellular or

molecular biological aspects. Analyzing physical properties in the lung have been considered important in understanding the pathology of lung diseases, and a couple of studies have been conducted by using computational or animal models^{16, 17, 18, 19, 20, 21, 22}. However, analysis of physical properties by on patient CT images with COPD, IPF, and left ventricular contractility in the animal model have not been performed before.

Speckle-tracking strain analysis has already been used²³⁻²⁵. Previous studies and reviews show that GLS and GCS are indicators of left ventricular (LV) function^{26, 27}. However, two-dimensional (2D) strain analysis has some limitations because it perceives the three-dimensional (3D) structure of the ventricles in only two dimensions²⁵. Theoretically, a 2D strain is unable to detect 3D cardiac motion because it cannot track the out-of-plane movement of the heart caused by rotational motion.

1-3. Outlines

This work aims to assess the physical framework for motion fields analysis from medical images with the basis of established image registration techniques. Applications on the medical images set of three diseases demonstrate the use of proposed methods to understand the cardiac and pulmonary function, adaptable either as of global, regional, or local approaches.

The thesis is organized as follows.

- Chapter 1 gives a brief introduction to the project and the specific aims. The background and related work of lung image registration and function estimation are also introduced.
- Chapter 2 proposes the mathematical and physical frameworks of physical motion analysis under the concept of continuum mechanics in detail.
- Chapter 3 provides some approaches to the lung and heart functions and progress revealing global and regional dynamic status or material properties.

2. Methods

2-1. Image Registration

Registration tracks the spatial mapping that aligns the moving images with the fixed images. Figure 2 showed the major components of the image registration framework. The input to the calculation is two images; one as the moving image I_1 and the other defined as the fixed image I_2 . The transformation is a spatial mapping of the points between the two images. The cost function represents the similarity measure of how well the fixed image is aligned with the interpolated moving image. This measure works as a quantitative queue to the optimizer over the search space defined by the transformation parameters. The interpolator calculated image intensities at non-grid positions using information from neighboring grid positions.

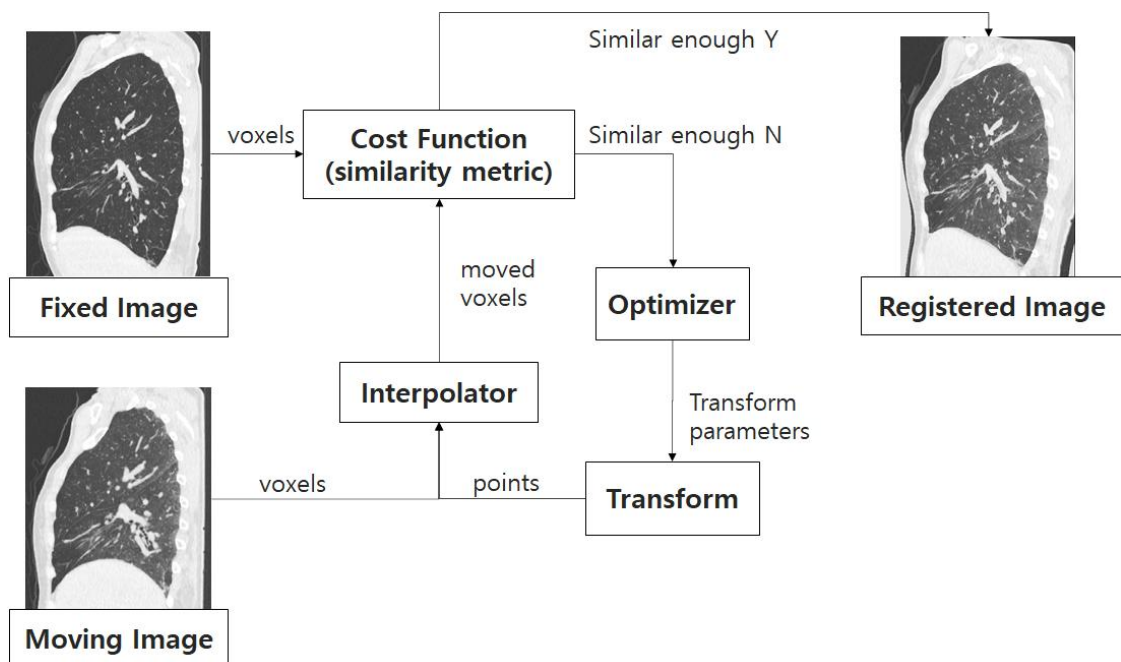


Figure 2. Framework for the image to image registration (example images: Lung CT)

For any given pair of image set, registration can be described as an optimization problem to find the transformation parameters μ which minimize the cost function – similarity measure – between the two image set as²⁸;

$$\mu = \arg \min C(\mu ; I_F, I_M)$$

where C is the cost function, μ parametrized transformation, I_F and I_M refers to the fixed and moving image, respectively.

(SW and libraries in the process) The preprocessing process – segmentation – in this study uses in-house software (AView, Coreline Inc. Korea). Three steps of transformation were sequentially engaged in registration of each case; Affine followed by B-spline and Level-set; to derive pixel-wise physical displacement map by combining the transformation results of three registrations. All three registration algorithms were implemented using ITK (Kitware Inc., Clifton Park, NY, USA); Affine and B-spline registrations with Elastix toolbox, and Level-set registration with `itkLevelSetMotionRegistrationFilter`²⁹. By the use of combined registration algorithms, physical motions medical images were tracked at every point of pixel center.

2-1-1. Preprocessing

(Mask segmentation - Depicting region of interest) Binary masks defining the region to be registered were calculated by image segmentation. Figure 3 showed an example of the original image and mask segmented by the thresholding for the lung CT image. The segmented mask could be divided into several sub-regions when a regional analysis is required, as in the example cases of figure 3, the segmented mask of lung CT be divided by left and right lung.

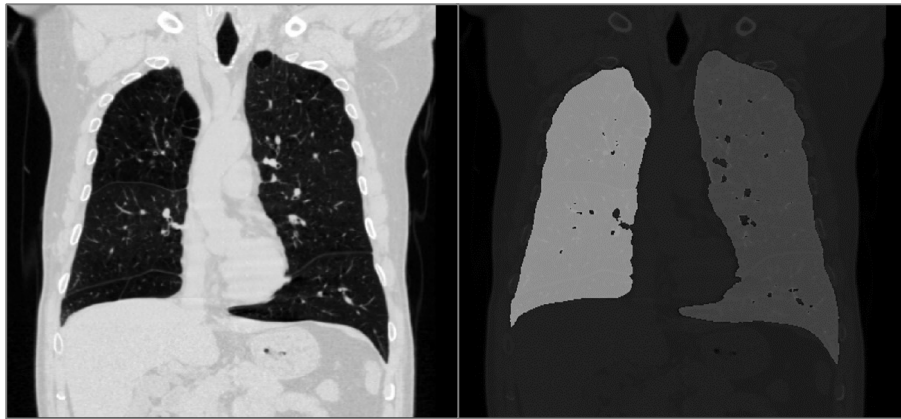


Figure 3. Example of image segmentation

(Histogram matching - Fitting the scale of original data) The pixel-wise brightness values in CT represent material density, which acts as an attenuation averaged in a given relative volume and defined as the Hounsfield unit (HU). Cardiac motion is derived from the contractile action of myocardial fibers, and negative pressure drives the pulmonary motion.

Both of the processes require the circulation of blood or air with the excessive volumetric changes. Thus, considering the partial volume effect of the medical image pixels, the attenuation of the same anatomical location changes during the motion of the lung or heart. This density change may reflect the actual volumetric changes of the local tissues, so shall be tracked via registration.

However, some portion of the density change between the two configurations in a single cycle of motion is a bias that alters the physical density change. In every measurement, image

acquisition, measurement-driven bias, and case-driven bias may alter the statistical distribution of the attenuation.

Thus, the distribution of the attenuation in every volume shall be normalized to exclude the possible bias resides in the images. In the normalization formula, windowing of the image visualization, flipping the sign of the negative typical HU values scale, shall also be considered as;

$$HU_{Normalised} = 1024 - 1024 [HU_{Original} - (WL - 0.5 \times WW)] / WW$$

where WL is window length, and WW is window Width.

Figure 4 describes the normalized process. The rational difference between original HU values to the window width span WW was expressed as $[HU_{Original} - (WL - 0.5 \times WW)] / WW$, then sign convention was flipped from negative to positive.

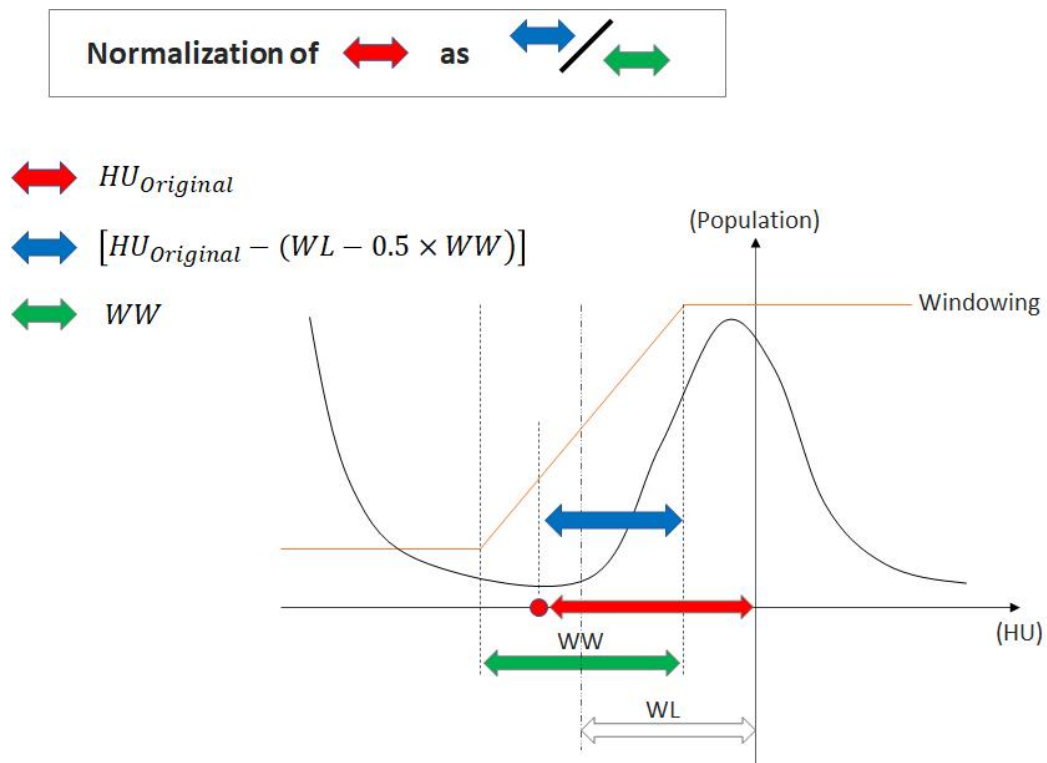


Figure 4. Concept of normalization in CT images

2-1-2. Cost functions (Similarity measures)

(Mutual information, MI) As one of the common choices among image similarities, mutual information was used to measure the similarity between images in iterative moving and the target image. ITK uses the definition given by Thevenaz and Unser³⁰ as below;

$$MI(\boldsymbol{\mu}; I_F, I_M) = \sum_{m \in L_M} \sum_{f \in L_F} p(f, m; \boldsymbol{\mu}) \log_2 \frac{p(f, m; \boldsymbol{\mu})}{p_F(f) p_M(m; \boldsymbol{\mu})}$$

where vector $\boldsymbol{\mu}$ is the transformation parameters, I_F and I_M are sets of regularly spaced intensity bin centers, p is the discrete joint probability, and p_F and p_M are the marginal discrete probabilities of the fixed and moving image, obtained by summing p over m and f , respectively.

2-1-3. Optimization

(Adaptive Stochastic Gradient Descent, ASGD) Solving the optimization problem in the former sections, commonly an iterative optimization strategy is employed to the parameterized transformation $\boldsymbol{\mu}$ as;

$$\boldsymbol{\mu}_{k+1} = \boldsymbol{\mu}_k + a_k \mathbf{d}_k, \quad k = 0, 1, 2, \dots$$

with \mathbf{d}_k the ‘search direction’ at iteration k , a_k a scalar gain factor controlling the step size along the search direction.

In selecting the ‘search direction,’ a negative gradient of the cost function can be selected as a trivial form as;

$$\boldsymbol{\mu}_{k+1} = \boldsymbol{\mu}_k - a_k \mathbf{g}(\boldsymbol{\mu}_k)$$

With $\mathbf{g}(\boldsymbol{\mu}_k) = \partial C / \partial \boldsymbol{\mu}$ evaluated at the current position $\boldsymbol{\mu}_k$

To solve this standard gradient descent optimizer, spatial points at the iteration step k shall be selected, and for the efficient convergence of the optimization and lighten the calculation load, the scalar gain factor needs to be set adaptively, so the iteration is stable enough but fast enough at the same time. Such an adaptive guess on the scalar gain factor can be added to the formulation of the iterative optimization, as described in the literature³¹.

2-1-4. Transformation

Transformation moves the points at the center of the voxels to the deformed space with the displacement field calculated at each iteration step. The transformation model defines the type of motion between the moving image and fixed image during registration.

(Affine transformation) A collective aspect of motion in linearized transformation can be expressed as ;

$$\mathbf{T}_{\boldsymbol{\mu}}(\mathbf{x}) = \mathbf{A}(\mathbf{x} - \mathbf{c}) + \mathbf{t} + \mathbf{c}$$

where $\mathbf{T}_{\boldsymbol{\mu}}$ is a non-parametric transformation at the point \mathbf{x} , with the amount of translation \mathbf{t} and rotation centered at \mathbf{c} , having no restriction on the matrix \mathbf{A} . This transformation model can accommodate any type of image flow including rotation, translation, stretch, shearing distortion unless the rate of moving surpasses linear regime.

(B-spline transformation) The amount of transformation exceeds the linear manner, which means the local material occupying the local image feature experiences severe and nonuniform motion in real-world, non-rigid and higher-order transformation formula is required. B-spline model provide transformation as ³²;

$$\mathbf{T}_\mu(\mathbf{x}) = \mathbf{x} + \sum_{\mathbf{x}_k \in N_x} \mathbf{p}_k \boldsymbol{\beta}^3\left(\frac{\mathbf{x} - \mathbf{x}_k}{\boldsymbol{\sigma}}\right)$$

With \mathbf{x}_k the control points, $\boldsymbol{\beta}^3$ the cubic multidimensional B-spline polynomial³³, \mathbf{p}_k the B-spline coefficient vectors (loosely speaking, the control point displacements), $\boldsymbol{\sigma}$ the B-spline control point spacing, and N_x the set of all control points within the compact support of the B-spline at \mathbf{x} . The control points \mathbf{x}_k are defined on a regular grid, overlaid on the fixed image.

(Level-set transformation) Vermuri²⁹ proposed the level set motion method for image registration. In this transformation model, an image moves along the direction of the gradient until it became similar to the target image.

The change of the motion field can be expressed as ³⁴;

$$dV/dt = (I_F - I_M(V)) \frac{\nabla I_M(V)}{\|\nabla I_M(V)\|}$$

where the motion field V is adjusted as ³⁴;

$$V_{n+1} = V_n + (dx/dt)\Delta t \quad | \quad V_0 = 0$$

where I_F, I_M is the fixed and moving image, respectively, V is the motion field, t is the temporal configuration. In the registration between two image set, t can be discretized as a single-valued scalar assuming the motion field incrementally varied as ΔV .

2-1-5. Interpolation

(B-spline interpolation) As the transformation proceeds for each iteration step, the points start from the center of the voxel move to the non-centered points in general. Thus, transformed points-grid requires interpolation in order to rearrange the transformation as the form of the voxel-to-voxel discrete mapping.

Several methods of interpolation exist from the linear to the higher-order, and in this study, 3rd order B-spline interpolation was used to occupy clear and smooth interpolation ³³.

2-2. The physical motion of a body

2-2-1. Concept of continuum media

Theoretical frameworks of applied physics focus on how “objects in nature” respond to the external load engagements. An external load may be any thermal, electromagnetic, mechanical, and nuclear potentials that can create flux at the boundary of the interested domain. A generalized mathematical description of the “object in nature” shall be considered to capture geometric and constitutive characteristics.

One of the generalized descriptions is the assumption of continuum. A continuum is an idealized status of materials that are composed of molecules separated by space, which molecules are “close enough” to propagate interactions by any provided external stimuli. The materials can exist as any of the solids, liquids, and gas phases, depending on the averaged distance of the molecules in the domain.

The importance of the continuum assumption lies in the reductionism of physical status. It assures transition of the information between molecules in microscale, thus in macroscale only the continuum body can be divided into elements keeping its material properties at each element with those of the average value in the entire domain. This ‘material property preserving’ assumption is the prime requisite for the designing, modeling, and predicting the physical analysis.

With the assuming of the continuum media, now an arbitrary point x within the physical body in space can be considered as a material point having physical properties, such as density, thermal capacity, etc. Then the motion of the physical body can be expressed in the form of mathematical equations, as most of the mathematical frameworks for the physical status inevitably include integral or differential operators.

2-2-2. Deformation vs displacement

Once linkage between mathematical expression and physical frameworks are set, the configuration, a body composed of the material points and formulated as the field variables at a specific coordinate and time, describes the status of the motion. For example, let's assume the cylindrical body rotates about its axis, then the body still occupies the same region in the space, whereas the motion exists in the form of rotation.

In general, when a material point has density – of course with a specific finite volume – experience arbitrary motion during the time from t_1 to t_2 , physical motion is expected to have 12 degrees of freedom(DOF). 6-dof in rigid body motions expressed as the displacement fields in the form of a 3-dimensional vector and 6-dof in the form of deformation expressed as strain fields in the form of 3-dimensional 2nd order tensor.

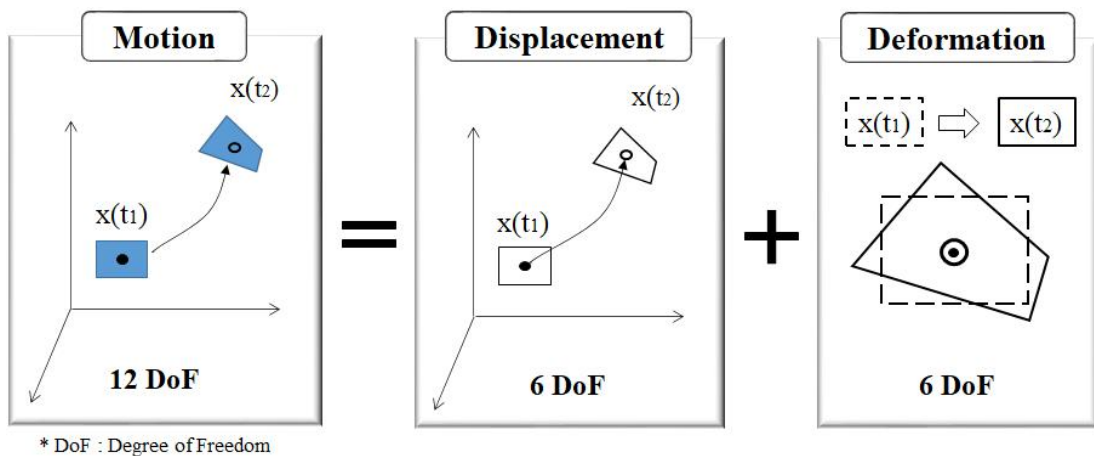


Figure 5. Descriptions on the physical motion of the material body, which can be decomposed into displacement and deformation.

(Characteristics of the deformation and displacement) A displacement of a material point is described as the portion of motion that preserves the relative distances with the

neighborhood points in the vicinity. On the contrary, deformation of a material point happens when there are certain changes in relative distances with the neighborhood points in the vicinity during the motion.

By the principle of the conservation, a body shows no change – motion – without the presence of the external load engaged. And once motion starts to happen, the physical properties work as inertia – a resistance – to the external loads.

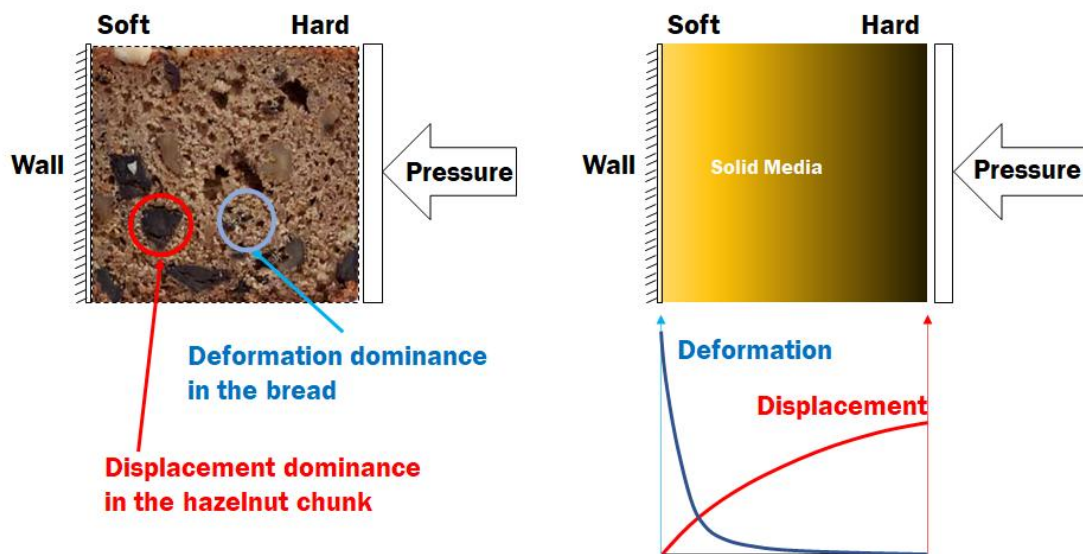


Figure 6. Example of the inhomogeneity in material properties; from the motion analysis by comparing the deformation and displacement

As an intuitive example, suppose a hazelnut chunked bread gets pressure load on one side and blocked in an opposite side, so it experiences motions. As the hazelnut chunk is stiffer than the bread media, almost all the deformation may happen at the material points of bread, whereas the majority of hazelnut chunks will just be displaced. As another example, if one changes the hazelnut chunked bread as a solid media having gradual stiffness change – softest part near wall and hardest part near the points of pressure loads. Almost all the deformation will predominantly be happened in the softest parts near the wall, whereas the displacement

will gradually be distributed in the entire domains.

Thus, from the observation on the portion of the two categories of the generalized motion – displacement and deformation – one may estimate the material properties at that specific material point. In medical imaging, this approach can be a non-invasive measurement of the structural compliance of internal organs.

2-2-3. Generalized expression of motion

In any specific configuration, a vector that connects arbitrary two material points P and Q in that configuration can be defined as in Figure 7. Then the deformation of the vector can be expressed as the changes in the length of the vector, whereas displacement of the vector can be expressed as the form of the translation of point P and rotation of the vector ³⁵. Recalling that the movement of every material point at the center of each voxel can be tracked between two or more configuration by the use of image registration algorithms, displacement field $u(x)$ of each material point can be defined at the location of pixel center in a specific configuration.

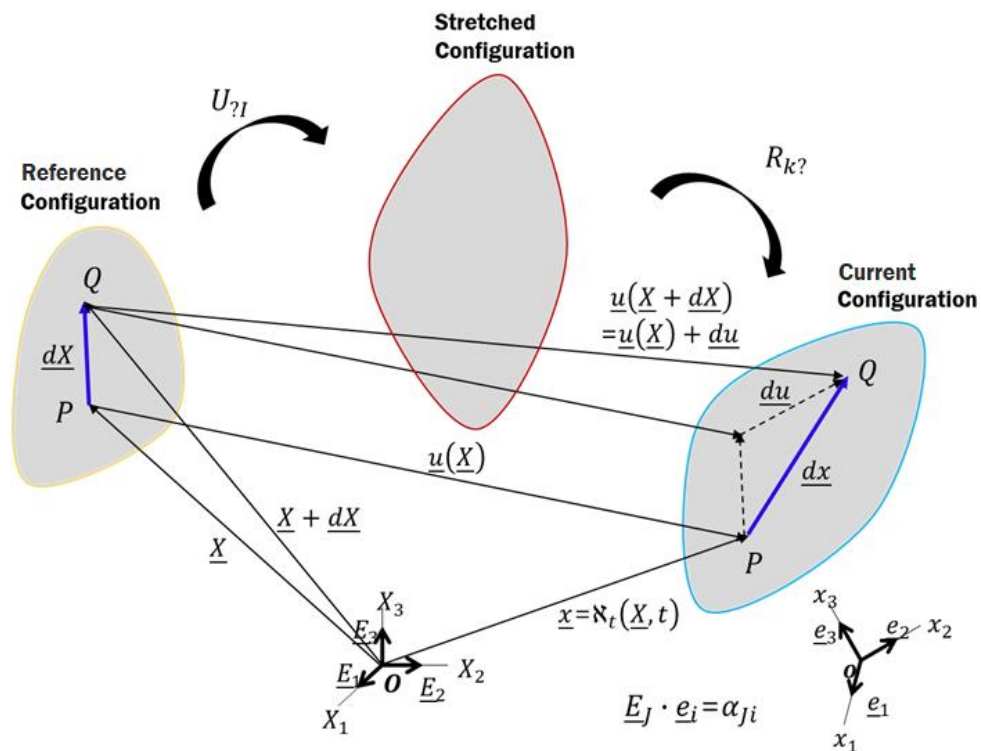


Figure 7. Physical body's configuration change (from undeformed to deformed, including rigid body motions) designed to separate deformation from the generalized motion

Under the displacement field prescribed by the function $u(X)$, index notation describes the location of an arbitrary point P in the inspiratory configuration as x_i , and in the expiratory configuration as X_A .

$$\begin{aligned} u_i(X_A) &= x_i(X_A) - X_A \\ u_A(x_i) &= x_A(x_i) - x_i \end{aligned}$$

(deformation gradient tensor) The deformation of a material point cannot be defined explicitly with only a point. As described before, relative distance change with the neighboring material point defines deformation, which expressed the deformation as to form of the gradient at a specific material point – defining deformation gradient tensor F_{iA} as,

$$F_{iA} \equiv \text{grad} x_i = \frac{\partial x_i}{\partial X_A} = x_{i,A}$$

Other derivation considering two points in each configuration can derive exactly the same formulation. Assume that the points P and Q are close enough at reference configuration and motions take the two points to the p and q at the current configuration, the segment pq can be expressed as;

$$dx_i = x_i(X_A + dX_A) - x_i(X_A)$$

Since p and q are neighboring particles, an approximation to this expression for small dx by the Taylor expansion gives

$$dx_i = \text{grad} x_i dX_A + O(|dx|^2) + \dots$$

then the relation between dx_i (vector PQ) and dX_A (vector pq) defines the deformation gradient tensor F_{iA} as,

$$dx_i = \frac{\partial x_i}{\partial X_A} dX_A = F_{iA} \cdot dX_A$$

$$F_{iA} \equiv x_{i,A}$$

One notion of this approximation is that there is no assumption that the deformation or deformation gradient is small; the only assumption is that the two material points p and q are close to each other. Thus, the deformation gradient keeps an arbitrary infinitesimal segmental sub-set of material points in reference configuration as a sub-set in the current configuration.

(Polar decomposition of deformation gradient tensors) As the deformation gradient tensor characterizes the gradient of the material points, the rigid rotational motion in the vicinity is included in the gradient of the point. To distinguish the effect of straining from the rigid rotation, imagine an intermediate configuration experiencing only the portion of the stretching from the reference configuration. Then the reference configuration experience transformation of pure stretches U, followed by the transformation of pure rotation R.

$$F_{iA} = R_{ib} U_{bA}$$

As the rotational transformation is proper orthogonal, thus transpose is its inverse.

$$R_{ib} R_{bj} = \delta_{ij}$$

Then pure stretch U can be expressed as below, so it can be characterized as ‘strain’ as in the following sections.

$$\begin{aligned} U_{AB} &= \sqrt{U_{Ab} U_{bB}} = \sqrt{U_{Ab} \delta_{bc} U_{cB}} \\ &= \sqrt{U_{Ab} R_{bi} R_{ic} U_{cB}} = \sqrt{F_{Ai} F_{iB}} \end{aligned}$$

2-2-4. Strain tensor as a deformation

2-2-4-1. Lagrangian strain tensor

In describing deformations, several strain tensors of deformation are commonly used. Considering one based upon the change during the deformation in the magnitude squared of the distance between the particles originally at P and Q, namely, where the symmetric tensor C_{AB} is called the Green's deformation tensor, just derived as in the previous section.

$$C_{AB} = x_{i,A} x_{i,B}$$

From this Green's deformation tensor, Lagrangian strain tensor E_{AB} can be defined in a one-to-one mapping manner to the pure stretch U.

$$2 E_{AB} = C_{AB} - \delta_{AB} = x_{i,A} x_{i,B} - \delta_{AB}$$

Then the Lagrangian strain tensor E_{AB} can be developed in terms of displacement gradients as followed.

$$\begin{aligned} 2 E_{AB} &= x_{i,A} x_{i,B} - \delta_{AB} = (u_{i,A} + \delta_{iA})(u_{i,B} + \delta_{iB}) - \delta_{AB} \\ &= u_{A,B} + u_{B,A} + u_{i,A} u_{i,B} \end{aligned}$$

$$\therefore E_{AB} = \frac{1}{2} (u_{A,B} + u_{B,A} + u_{i,A} u_{i,B})$$

Now the displacement field $u(x)$ at the location of pixel center in inspiratory configuration can be used to calculate Lagrangian strain tensor E_{AB} , representing the deformation of each material point.

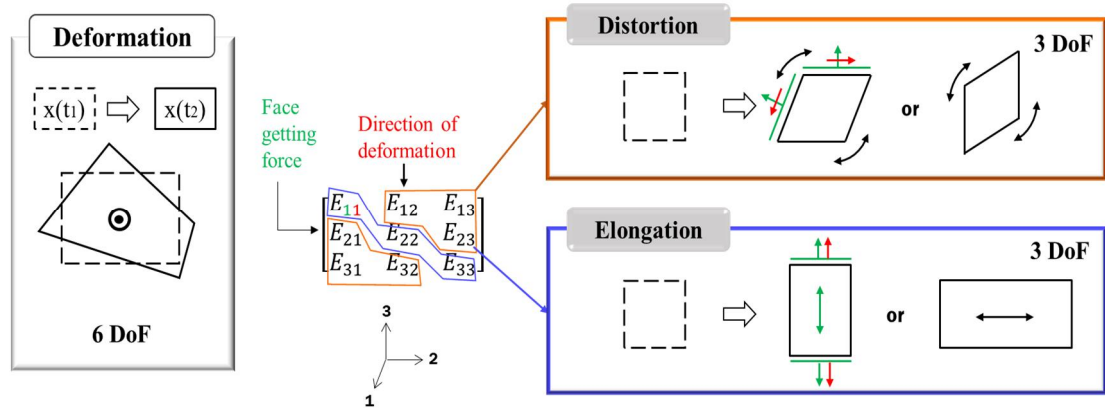


Figure 8. Types of the deformation in stain tensor, defined by the combination of the two directional basis

The strain tensor is 2nd order tensor having two directions related to its 9 components, and the physical implications are the direction of the deformation, and the direction of the face normal to the load exerted, respectively.

The strain tensor has 6 independent elements by the symmetric formulation, which implies 6 degrees of freedom related to the deformative portion of the generalized motion. As in the figure 8, off-diagonal elements represented distortive behavior and expressed as the symmetric pair components as the couple effects of shearing, whereas the diagonal element of strain represents the elongations as the direction of the deformation is aligned to the direction of face average getting load.

2-2-4-2. Infinitesimal versus finite strain

The generalized expression to the components of strain tensor derived in the former section can be applied to any scale of deformation unless the continuum assumption is broken.

$$\therefore E_{AB} = \frac{1}{2} (\mathbf{u}_{A,B} + \mathbf{u}_{B,A} + u_{i,A} u_{i,B})$$

Adding the assumption to the generalized terms that the deformation is small enough relative to the original length scale, multiplicative higher-order terms $u_{i,A} u_{i,B}$ in the right-hand side can be ignored as the gradient value shall be smaller than unity;

$$\therefore E_{AB} = \frac{1}{2} (\mathbf{u}_{A,B} + \mathbf{u}_{B,A}) \quad (\text{for infinitesimal deformation})$$

Most of the metallic materials showed a relatively small amount of deformation when compared to the characteristic length of the original body. Thus, this assumption of ‘infinitesimal’ strain can be an efficient way of calculation without the loss of the major deformative features in the calculation.

However, in the lung and heart motion, the amount of deformation is excessive such that the order of magnitude for the deformation is merely the same with that for the length scale of the domain. As an example, in a healthy subject, total lung capacity at the forced inspiration is 6.0 liters, and residual volume at the forced expiration is 1.2 liters in men³⁶. Also, heart ejection fraction, the volumetric fraction of blood flow ejected from the heart chamber, is 66 to 67%³⁷.

Thus, in the analysis of the biomechanical motion of the lung or heart, the formulation of the deformation must follow the generalized formulation considering large – finite – deformation of the target organ.

2-3. Assessment of physical motion

2-3-1. Volumetric changes

(Volumetric strain) The volumetric changes of a material point can be calculated from the strain tensor as;

$$E_{AB} = \frac{1}{2} (u_{A,B} + u_{B,A} + u_{i,A} u_{i,B})$$

The volumetric changes of a material point can be calculated from the volume increments of reference configuration dV_0 and dV , respectively;

$$\begin{aligned} dV_0 &= d\mathbf{Z} \cdot (d\mathbf{X} \times d\mathbf{Y}) = \varepsilon_{ABC} dX_A dY_B dZ_C \\ dV &= d\mathbf{z} \cdot (d\mathbf{x} \times d\mathbf{y}) = \varepsilon_{ijk} dx_i dy_j dz_k \end{aligned}$$

Considering the deformation gradient tensor yields,

$$dV_0 = \varepsilon_{ABC} dX_A dY_B dZ_C$$

$$\begin{aligned} dV &= \varepsilon_{ijk} dx_i dy_j dz_k = \varepsilon_{ijk} (x_{i,A} X_A) (y_{j,B} Y_B) (z_{k,C} Z_C) \\ &= \varepsilon_{ijk} x_{i,A} y_{j,B} z_{k,C} X_A Y_B Z_C = \varepsilon_{ABC} \det(\mathbf{F}) X_A Y_B Z_C \\ &= \det(\mathbf{F}) dV_0 \end{aligned}$$

$$\frac{dV}{dV_0} = \det(\mathbf{F})$$

In the case of no coordinate transformation between the configuration, deformation gradient tensor expressed in terms of the displacement fields can be simplified into single coordinate indices as;

$$\begin{aligned}
F_{iA} &= x_{i,A} = u_{i,A} + \delta_{iA} \\
&= x_{i,j} = u_{i,j} + \delta_{ij}
\end{aligned}$$

Such assumption provides Jacobian determinant of the deformation gradient tensor as;

$$J = \det \left[\frac{\partial x_i}{\partial X_A} \right] = \det \left[\frac{\partial u_i}{\partial X_A} + \delta_{iA} \right]$$

$$J = \det \left[\frac{\partial x_i}{\partial X_j} \right] = \det \left[\frac{\partial u_i}{\partial X_j} + \delta_{ij} \right]$$

Note that this assumption on the coordinate transformation could have a bias on the calculated strain values as the coordinate transformation matrix between reference and the current configuration cannot always be identical in practice. This compatibility compensation is one of the key issues of errors in regarding the calculation of the displacement fields via image registration.

From this analytic formula of Jacobian, the level of approximations simplifies the terms of volumetric change into a different level of non-linearity; infinitesimal strain and large deformation.

(Infinitesimal volumetric strain) Infinitesimal strain assumes that the deformation is small enough to ignore all the multiplicative higher-order terms, including quadratic and cubic terms. In this case, the volumetric change can be approximated into the 1st invariance of the strain tensor.

$$J = \det \begin{bmatrix} \frac{\partial u_1}{\partial X_1} + 1 & \frac{\partial u_1}{\partial X_2} & \frac{\partial u_1}{\partial X_3} \\ \frac{\partial u_2}{\partial X_1} & \frac{\partial u_2}{\partial X_2} + 1 & \frac{\partial u_2}{\partial X_3} \\ \frac{\partial u_3}{\partial X_1} & \frac{\partial u_3}{\partial X_2} & \frac{\partial u_3}{\partial X_3} + 1 \end{bmatrix} \approx \frac{\partial u_1}{\partial X_1} + \frac{\partial u_2}{\partial X_2} + \frac{\partial u_3}{\partial X_3} + 1$$

$$\frac{dV}{dV_0} = J - 1 \approx \frac{\partial u_1}{\partial X_1} + \frac{\partial u_2}{\partial X_2} + \frac{\partial u_3}{\partial X_3} \text{ (for infinitesimal deformation)}$$

(Finite volumetric strain) Multiplicative higher-order terms survive in the case of the finite deformation, and the simplification level drops to the extent of quadratic terms survived, so the entire behavior resides in the non-linear regimes.

$$J = \det \begin{bmatrix} \frac{\partial u_1}{\partial X_1} + 1 & \frac{\partial u_1}{\partial X_2} & \frac{\partial u_1}{\partial X_3} \\ \frac{\partial u_2}{\partial X_1} & \frac{\partial u_2}{\partial X_2} + 1 & \frac{\partial u_2}{\partial X_3} \\ \frac{\partial u_3}{\partial X_1} & \frac{\partial u_3}{\partial X_2} & \frac{\partial u_3}{\partial X_3} + 1 \end{bmatrix} \approx \left(\frac{\partial u_1}{\partial X_1} + 1 \right) \left(\frac{\partial u_2}{\partial X_2} + 1 \right) \left(\frac{\partial u_3}{\partial X_3} + 1 \right)$$

$$\frac{dV}{dV_0} = J - 1 \approx \left(\frac{\partial u_1}{\partial X_1} + 1 \right) \left(\frac{\partial u_2}{\partial X_2} + 1 \right) \left(\frac{\partial u_3}{\partial X_3} + 1 \right) - 1$$

(for finite deformation)

2-3-2. Principal strain

(Eigenvalue problem) the invariance of the strain tensor can always be found, as the continuum assumption provides non-zero value for the determinant of the deformation gradient tensor. Also, with the use of the eigenspace span, one can always find the rotational coordinates transform L such that the transformed strain tensor has non-zero values only for the diagonal elements.

$$E_{AB} = L_{AC} P_{CD} L_{DB}$$

Where

$$E_{AB} = \begin{bmatrix} E_{11} & E_{12} & E_{13} \\ E_{21} & E_{22} & E_{23} \\ E_{31} & E_{32} & E_{33} \end{bmatrix}, P_{CD} = \begin{bmatrix} P_1 & 0 & 0 \\ 0 & P_2 & 0 \\ 0 & 0 & P_3 \end{bmatrix}$$

The degree of freedom on the deformation seemed to be lost, however, does not compromise even if the principal component analysis proceeds as the 3 base vectors for rotated axis takes 3 degrees of freedom for the non-trivial eigenspace.

2-3-3. Equivalent strain

(Concept of yield and its criterion in applied physics.) The yielding phenomenon is observed in material science that the body exceeds the limit of elastic deformation regime and starts to permanently plastically deforms under the certain direction of mechanical loads.

Various pieces of literature provide isotropic and anisotropic yield³⁸⁻⁴⁰, and all the criteria mentioned above propose cumulative, scalar measures of deformation for each material point by the calculation of the elemental operation on the stress tensor. The majority of the scalar cumulative measures are associated with the invariances of the strain tensor, so the mathematical frameworks minimally affect the physical results.

Though the stress tensor is one of the potentials that create motion in the form of the strain, the concept of the yield and equivalent has widely been used to describe the representative state of solid deformation as a scalar value. As this measure refers to the detaching condition of atomic alignment, it is expected to be a measure implying a biomechanical mismatch between performance needs and functional capacity.

In this study, the most common form of yield criterion, Von-Mises equivalent strain, for the isotropic media were calculated as an example assessment.

Von-mises equivalent criterion assumes that the yielding occurs when the second invariance of deviatoric stress J_2 reaches a critical value and provides the best fit to predict the yielding of the ductile materials.

Deviatoric part D of a strain tensor E can be described as;

$$D_{AB} = E_{AB} - \frac{1}{3}E_{CC} \delta_{AB}$$

Then the equivalent Von-Mises strain is formulated as below.

$$\begin{aligned} EVM &= \sqrt{\frac{(E_{11}-E_{22})^2+(E_{22}-E_{33})^2+(E_{33}-E_{11})^2+6(E_{12}^2+E_{23}^2+E_{31}^2)}{2}} \\ &= \sqrt{\frac{(P_1-P_2)^2+(P_2-P_3)^2+(P_3-P_1)^2}{2}} \\ &= \sqrt{\frac{3}{2}D_{AB}D_{AB}} \end{aligned}$$

2-4. Sources of bias

2-4-1. Bias in registration

(Continuity condition on image intensity) Two out of three transformation models used in the study calculates gradient across the domain of the volume image, as described in 2-1-3.

In the case of the level set transformation, as the model engages the part of the motion projected to the direction of the gradient, the use of the gradient can provide efficiency of calculation over the typical optical flow. However, the use of gradient also requires a high level of continuity for the field variables, which means, in reverse, it can easily fall to the local minima, and the resultant registered image may have a lack of smoothness. Not only the level set model but any of the model using gradient calculation sharpen the data field inevitably. In other words, if an algorithm is non-linear, non-rigid, and fast by the use of the gradient-based formulation, it requires a higher quality of original image itself. However, the necessity of high-resolution images typically comes from the complexity of the target organ, with the high possibility of noise and artifacts.

(Selection of the transformation parameters) To compromise the performance of the registration as described above, adaptation techniques on the initial guessing, sampling size, iteration step, are well established in the literature^{31,34}.

For each study, thus, for each imaging modality and imaging protocol, it is recommended to explore the transformation parameters that provide the optimal performance aligned to the purpose of the study.

2-4-2. Bias from mode and scale of motion

(assumption bias by the small and large deformation) As described in the 2-3-1, the level of the approximation for higher-order terms must be controlled to capture the deformation intact, especially in the calculation of the volumetric changes. Figure 9 showed the variation of the volume in real (top) and the approximated one (bottom): bottom left green line showed the calculated volume change only when linear terms engage. The bottom right yellow line showed the ignored volume contribution via higher-order terms.

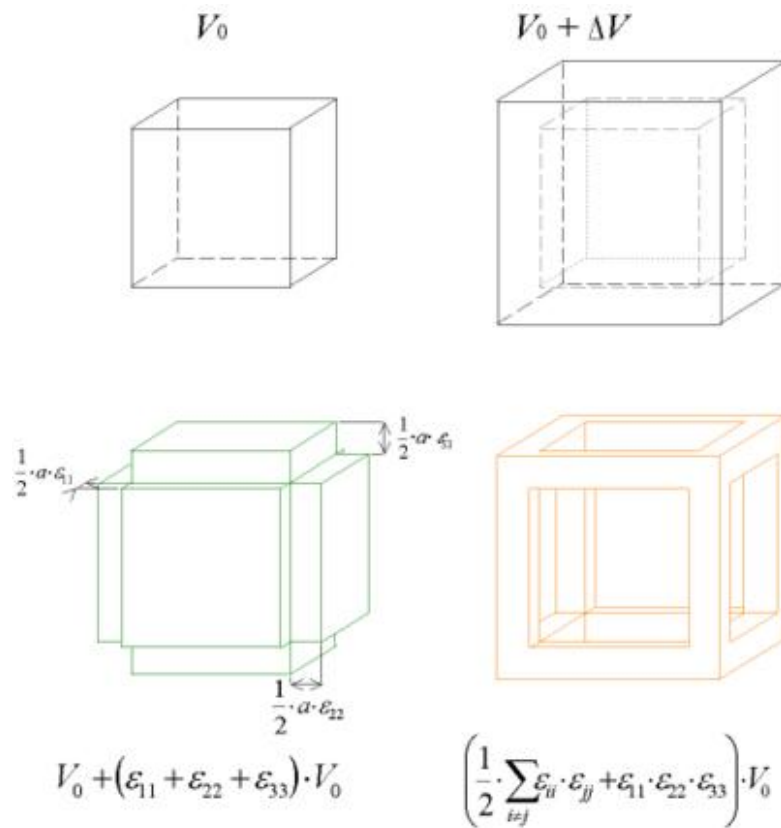


Figure 9. Physical body's configuration change (from undeformed to deformed, including rigid body motions) designed to separate deformation from the generalized motion.

Recalling that the formula of the volumetric change in the case of the infinitesimal strain and finite strain, up to the 3rd order terms, could be introduced to the calculation of volume

change.

$$\frac{dV}{dV_0} = J - 1 \approx \frac{\partial u_1}{\partial X_1} + \frac{\partial u_2}{\partial X_2} + \frac{\partial u_3}{\partial X_3} \quad (\text{infinitesimal deformation})$$

$$\frac{dV}{dV_0} = J - 1 \approx \left(\frac{\partial u_1}{\partial X_1} + 1 \right) \left(\frac{\partial u_2}{\partial X_2} + 1 \right) \left(\frac{\partial u_3}{\partial X_3} + 1 \right) - 1 \quad (\text{finite deformation})$$

(Gradient typed calculation) With the same aspect of 2-4-1, the calculation of deformation gradient tensors also lowers the image continuity and introduces the high-frequency noise. Not like the case in registration, discontinuous value calculates from the physical analysis can be converted and compared to the ground truth. However, the calculated tensor field can be altered by the postprocessing as smoothing, which is necessary for the compensation of the gradient-based calculation steps.

2-4-3. Smoothing

(Smoothing the calculated deformation) Smoothing at the final stage of the calculation of motion plays a mathematical counter effect of the gradient-based above calculations, as mentioned in the previous section.

Also, the physical body motion-tracked from the image registration has a typical error by the scale of pixel size. Bronchial lines and vessels in **the** lung shall certainly be an exceptional change in compliance, thus smoothing the high-frequency noise patterns is highly recommended.

Thus, all the deformation calculated from image registration in this study was processed with the gaussian smoothing filters by the depth of 3 pixel ⁴¹.

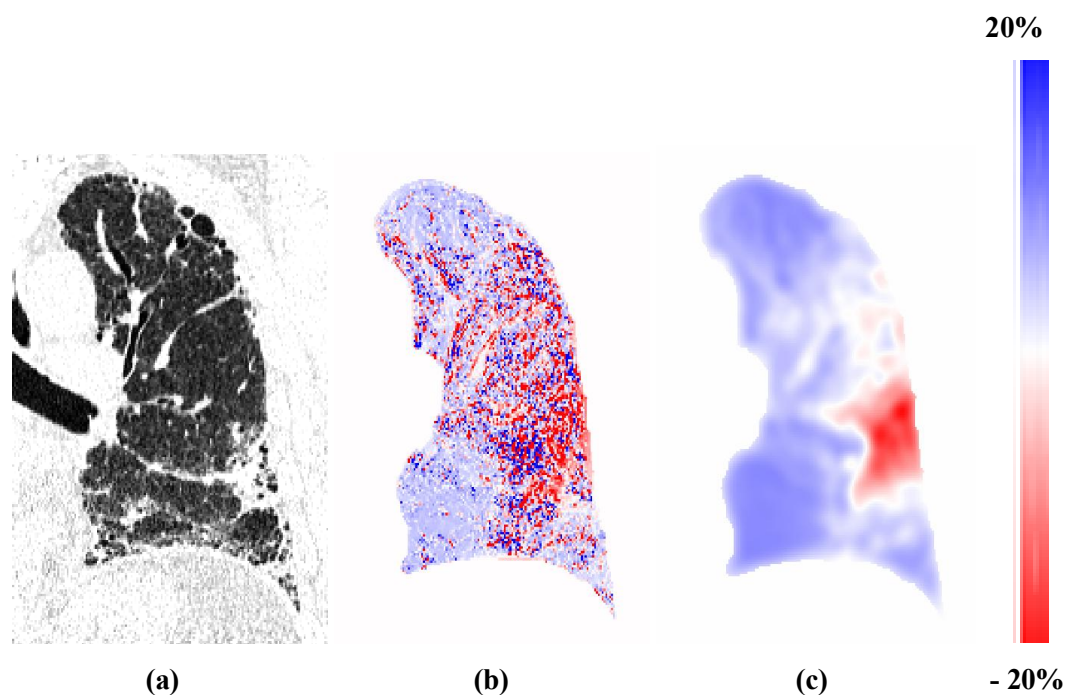


Figure 10. Example of smoothing on volumetric deformation (AAVC%) during inspiration; lung CT image at inspiration; (a) raw medical image, (b) unsmoothed volumetric deformation, (c) smoothed volumetric deformation by gaussian filter with 3-pixel depth.

2-4-4. Bias scales in each calculation steps

(Scales in image registration) As described before, mutual information following the definition given by Thevenaz and Unser³⁰ was used to measure the similarity between the image in iterative moving and the target image. Table 1 showed the mean and standard deviation of mutual information calculated from the registration of randomly selected 1 one 6 portions of study cases for COPD and IPF.

Table 1. Mutual information calculated from the registration of randomly selected 1 one 6 portions of study cases for COPD and IPF.

Data selected	Mutual Information
	Mean \pm Standard Deviation (SD)
10 COPD cases	0.41 \pm 0.06
5 IPF cases	0.26 \pm 0.13

Though the mutual information provides a convergence condition as a similarity measurement for the registration process, it does not provide the accuracy for the motion in length scale. One such measure is target registration error (TRE), a Euclidean distance between the corresponding landmarks in the target and moving images. Considering the bias from the disease features in the image, a manual annotation for the landmark is recommended to be acquired via professional radiologists. Literature provides typical TREs for lung registration as followed. Hualiang Zhong et. al. showed the B-spline registration of 10 lung CT pairs had average \sim 1.5 mm TRE with the parameter optimization⁴², Jan R uhaak et. al. showed various state-of-the-art deformable registration algorithms showed 0.58~3.29 mm TRE in average for for DIR-LAB COPD Datasets⁴³, Piotr Swierczynski et. al. showed the level-set based joint segmentation and registration algorithm provide the best TRE of 3.40 in average for the 10

pairs of complete 4D CT lung scans of patients suffering from lung or esophageal cancer ⁴⁴.

Also, as a direct reference for the deformable registration algorithms in this study, Daegwan Kim et. al. provided comparisons of 4 deformable registration algorithm including level-set, Demons, Diffeomorphic demons, B-spline by the visual scoring of the professional radiologist and image similarities. Level-set registration algorithm showed the highest visual scoring by the clinical experts and the lowest similarity errors ⁴⁵.

Thus, the deformable registration algorithms are currently shown to have approximately 3 mm TRE, though it may depend upon the raw image qualities and parameter optimization. Counting that the voxel size of the typical cases in Lung CT and Echocardiography as ~1 mm, the typical value of TRE as 3 mm implies that the local spatial changes within less than 3voxels are not recommended to analyzed as ‘signal’ with significance.

(scales in motion of target domain) The accuracy of the lung motion in voxel scale cannot be determined without measured ground truth as the ultra-resolution CT tracking for ex-vivo lung specimens, which is not covered by this study.

As an alternative to the truth measured by the strict biological experiment and micro CT acquisition, the analytic approach could provide the maximum scale of possible error exist. Recalling that the strain tensor of a material point can be calculated from the strain tensor as;

$$E_{AB} = \frac{1}{2} (u_{A,B} + u_{B,A} + u_{i,A} u_{i,B})$$

Assuming that the maximum error in the displacement field at the voxel center can be scaled as the 3 voxels – that be ~ 3 mm in approximation. As the differentiation in the formula can be discretized into voxel-wise differences with the neighboring voxels, the effect of the error that can be engaged depends on the difference of displacement between neighboring voxels.

The typical scale of left or right lung size be a hundred to few hundred mm in length. Thus let's consider the worst cases that the neighboring two voxels had a maximum error of 3 mm via image registration, even though such case hardly happens except for the boundaries of the regions of interest as the interpolation between two physical status shall correlate the motion of the neighboring voxels in a closer fields values. Nevertheless, maximum possible error $e(u_{A,B})$ for the displacement gradient $u_{A,B}$ can be approximated up to 3%. Counting this 3% as a maximum error for $e(u_{A,B})$ in the calculation of the strain tensor E_{AB} and it's error $e(E_{AB})$ yields,

$$\begin{aligned}
& E_{AB} + e(E_{AB}) \\
&= \frac{1}{2} ([u_{A,B} + e(u_{A,B})] + [u_{B,A} + e(u_{B,A})]) \\
&+ [u_{i,A} + e(u_{i,A})] [u_{i,B} + e(u_{i,B})] \\
&= \frac{1}{2} (u_{A,B} + u_{B,A} + u_{i,A}u_{i,B} + [e(u_{A,B}) + e(u_{B,A})]) \\
&+ [u_{i,A}e(u_{i,B}) + u_{i,B}e(u_{i,A}) + e(u_{i,A})e(u_{i,B})]
\end{aligned}$$

$$\begin{aligned}
e(E_{AB}) &= e(u_{A,B}) + e(u_{B,A}) + u_{i,A}e(u_{i,B}) + u_{i,B}e(u_{i,A}) + e(u_{i,A})e(u_{i,B}) \\
&\cong 6.9\% + 3\% (u_{i,A} + u_{i,B}) \cong 10\%
\end{aligned}$$

Considering the displacement gradient value $u_{i,A}$ typically cannot exceeds 0.5, the maximum error in the tensor E_{AB} calculation can be 10% of its strain value. As in the large deformation the strain value is typically 0.2~0.4, the error in strain can be 0.02~0.04.

Thus, strain-based calculations could have relative error up to 10% as a maximum, which implies that robust physical measures are recommended to define in the sub-regional domains, around the scale of few to several voxels. However, as described before, error in the displacement gradient field hardly reaches the value of 3% except for the boundaries of the region of interest.

(Range of meaningful analysis) In considering the error scale assessed in the current sections, it is suggested that in the analysis of deformation from the image registration technique

1. Field values shall be understood as regional or sub-regional trends rather than as a voxel-wise precise value. Smoothing at the least of 3 voxels is recommended to counter the registration error.
2. Error driven by the calculation of the deformation cannot be estimated precisely without the Ex-vivo CT scans for the lung specimen. The scale analysis suggested the maximum error bound as the 10% of the strain tensors value, noteworthy that the error bound described is the mathematical & physical maxima from the calculation formula of deformation.

2-5. Contribution and Implication

2-5-1. Pixel-wise motion in full (12) degree of freedom

In this thesis, the constitutive frameworks describing the physical motion from the medical images were formulated in the form of the analytic equations. With this ideation, one can independently separate any type or aspect of physical motion either in local(voxel-wise), regional, global domain. Though the process of this calculation is relatively complicated, sources of bias at the key steps of the calculation are described to prevent the cumulation of errors.

2-5-2. Physical regime for ‘large’ deformation

The analytic, generalized constitutive formula preserved primitive higher-order terms intact, thus depending on the scale of the motion, the effective range of approximation can be applied, such that the scale of the error for the deformation can be controlled below the size of the characteristic length scale, i.e. voxel size in medical images.

2-5-3. Clinical implication on each degree of motion

(Why ‘deformation’ on lung and heart) Each of the 12 degrees of freedom in the physical motion of a body can be categorized as;

1. Displacement : 3 degrees of freedom, three directions in cranio-caudal / anterior-posterior / left-right axis
2. Rotation : 3 degrees of freedom, rotation about each 3 axes, dependent to structural connectivity, material stiffness, external load, and their combination.

Rotation may not be critical in solids.

3. Deformation : 6 degrees of freedom, following the 3 directions of the load exerted and the 3 directions of the face of load exerted. Symmetric formulation explained in the section 2-2-4 make the degree of freedom into 6, not 9. Each of the elements in the strain tensor may not intuitively interpret the organ function or to mechanical stress loaded to the tissue. Thus, depending on the target organ be analyzed, the category of the mechanical strain analysis shall be defined in adequate portions that reflect the organ function and portions that do not.

Among the above-mentioned degrees of motion, it was speculated that the portion of the deformation term that does not serve for organ function has the most important clinical implication. Lung and heart are organs whose functions are material exchange, lung for gas exchange, and heart for blood. Displacement and rotation have nothing to do with the material exchange, and only parts of deformation term serve for gas/blood exchange, whereas the rest of the deformation term does no good for function but exerts mechanical stress to the tissue.

Lung and heart have fibers and walls as functional units. The elastic recoil of the fibrous tissues is essential for normal function, but elastic recoil of the fibrous tissues decay upon the repeated loading of mechanical stress. Cells and the ECM in the lung are under the influence of transpulmonary pressure and the incessant mechanical stresses of breathing¹⁴. Figure 11 is quoted from Suki et al.'s review on the role of mechanical stress-induced lung remodeling and modified for demonstration. In the schematic figure, breathing motion exerts '3-D deformation as a continuum' to walls and fibrous tissue to let them stretch, that may directly rupture the fibers or walls, or induce mechanotransduction pathway both would lead to excess inflammation. Fragmented fibers in rupture could also induce inflammation. Irritants such as cigarette smoke and pollutants and patient-specific genetic background play their roles in these pathways to inflammation. Pathogenic CT observations based on HU values such as low/high

attenuation areas represent the extent of fiber or wall failure, as denoted with a green arrow.

On the contrary, the measurement of mechanical stress focuses on the upstream of this pathway.

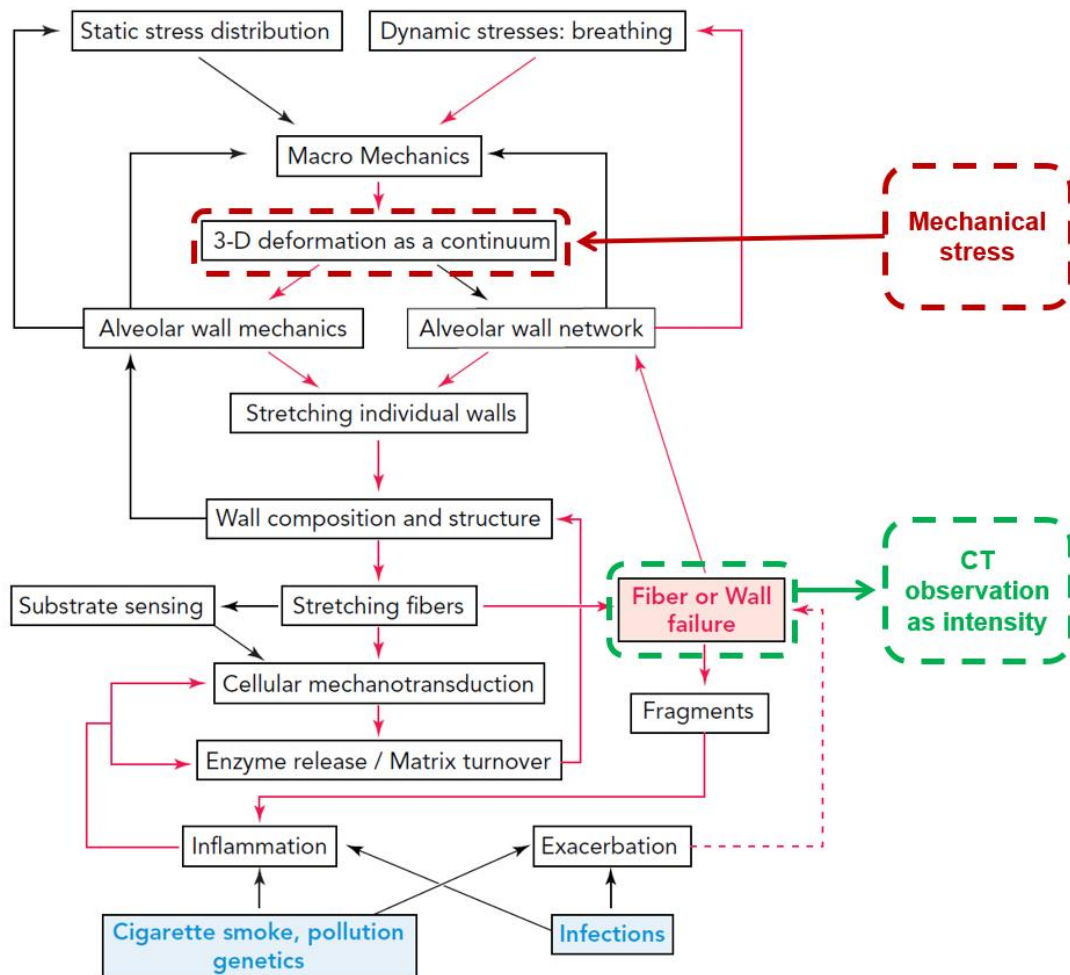


Figure 11. Schematic diagram showing the role of mechanical stress-induced lung remodeling (modified, figure 1 of literature ¹⁴)

(Selection of strain measure in pulmonary and cardiac analysis) As describe above, review literature point the view that the mechanical/physical load engaged in the tissue affects the status of the inflammation, which leads to the instability of ECM remodeling as results ⁴⁶, ¹⁴. Indeed, macroscopic mechanical strains exert stress on the collagen network in the microscopic scale. Combining recent studies on laboratory animals ⁴⁷ and computational models, ⁴⁸ emphysematous lesions were under severer mechanical stress.

However, still, there is no defined consensus on the use of the mechanical load as a biomarker in the analysis of the local tissue remodeling and clinical application. Some researches even do not provide decent stratification on the type or on the direction of the strain, in the analysis of load concentration ⁴⁸, ⁴⁹.

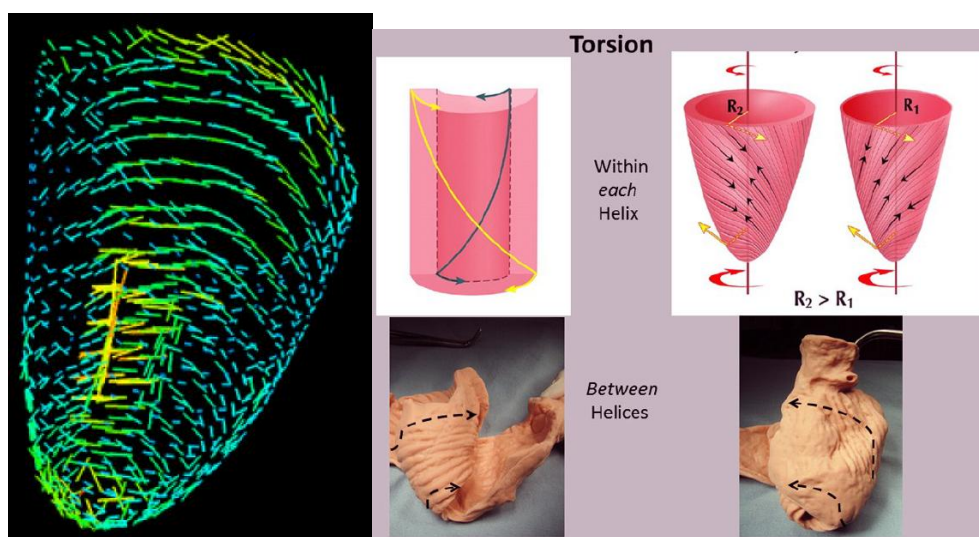
Following the rigorous notation and data comparison scheme in physics, analysis of the field variable in the spatial domain is recommended to compare either ‘direction based’; with the specific element of the tensor or vector to align the comparison in the same direction of motions, or ‘regime based’; with invariance scalar values of the target tensor or vector to counter the directional span. Table 2 explains suitable categories of analysis for each application in the next sessions.

Table 2. Categories of strain analysis; vector-based (direction) vs scalar-based (regime)

Strain analysis categories		Fitness of analysis	
Major	Sub	In Lung	In Heart
Direction based	Directional	Inappropriate (global direction does not represent major portion of the motion)	Sub-optimal (global direction represents some portion of the motion however with defects)
	Principal	Inappropriate (Source of motion is diaphragm, not lung parenchyma)	Appropriate (Reflection of active contraction of myocardial fibers)
Regime based	Volumetric	Appropriate (Reflection of ventilation function)	Inappropriate (cardiac wall is tracked, and cavity is out of the ROI)
	Deviatoric	Sub-optimal (deformation with volume change also affect the amount of the stress in the local tissues)	Inappropriate (combining the major source of contraction – deformation in the principal direction – with other element may alter the results)
	Effective	Appropriate (Reflection of total amount of the mechanical stress in the local tissues)	

(Direction-based analysis for cardiac motion) Choosing the global direction of motion, such as axial, coronal, sagittal in the radiologic field as a strain analysis, is not recommended when considering the anisotropic biomaterial patterns in the pulmonary and cardiac tissue textures and structures for one-way blood flows. None of the primal elements of motion fits with the global directions; driving source of motion, structural characteristics, spatial spread of material properties, etc. However, cardiac motion can be analyzed effectively with one of the direction-based measures, the principal strain, which follows the direction of the biggest deformation exerted for each voxel, thus can follow the reflection of the myofibril contraction in the cardiac wall. And the thickness of the cardiac wall is changed as a passive compensation for the mass conservation during the myofibril contraction. Thus, summing up the effects at a specific point into any form of the scalar invariance can alter the amount of the driving source for the cardiac motion. Figure 12 showed the direction of the principal strain representing the contractile motion of myocardial fibers.

Though the cardiac wall described the blood-flow functions as ejection fraction, the portion of the strain analysis is defined only on the wall, not in the cardiac cavity; thus any of the measures in the form of the scalar value hardly reflects the cardiac function.



(a)

(b)

Figure 12. (a) The direction of the principal strain calculated in the normal beagle with the speckle tracking point-grid from echocardiology, representing the contractile motion of myocardial fibers, (b) the helical anatomy and biomechanical direction of motion ⁵⁰.

(Regime-based analysis for pulmonary motion) In lung motion, on the contrary, the diaphragm contraction and relaxation, with the help of the muscles surrounding the chest cavity, drive the volume change of chest cavity and thus drive negative pressure to induce airflow. Physically, the motion of parenchyma is passive results of the negative pressured made by the chest wall motion. Thus, not only in the global coordinate but also in principal, the direction of motion in lung parenchyma does not imply any of the significant dynamics in the tissues. The resultant feature is rather the combination of structural complexity with the branched patterns and the pathophysiology-driven compliance changes.

In the case of the lung, a sub-grouping of the tensor variable into scalar invariances is recommended following the type of the physical effect. Table 2 explains the sub-grouped scalar invariance and its physical and physiological implications.

As described above, the source of the dynamic motion is not intrinsic in the lung parenchyma. In detail, firstly, the motion of the chest wall induces the passive change of lung volume in a global scale, and the effect of load concentration is followed by the morphology of the structures and the compliance distribution of the local tissues.

Thus, the major portion of the physical motion in the lung firstly be the local volumetric changes and followed by the representation of the total load engaged in the tissue. The distortive portion of the strain, having no volumetric strain, might be one of the options as a common counter portion of the volume changes, however, as the portion with the volumetric change also contributes the mechanical damage of the biomaterials, the total amount of the mechanical strain – effective strain – is the primal measure to analyzed. In this study, the effective strain, as a total amount of the mechanical load, was expected to represent the amount

of the destruction source for the ECM fibers, which leads to the inflammation happened in the local tissues.

This over-inflammation causes not only the abnormal reconstruction of the tissue structures in microscale, but also causes the typical symptoms of COPD or IPF patients in macroscale ⁵¹. As the symptoms were developed, the patients will experience pain and inconvenience in breathing, which leads the patient to various mal-adaptation as anterior bent posture, decrease in the range of respiratory motion, shortness of breath, etc. It was speculated that the differences between the volumetric changes and effective strain help the understanding on the mal-adaptation, with no matter how rapid the progress of the disease is, or how severe the disease status is.

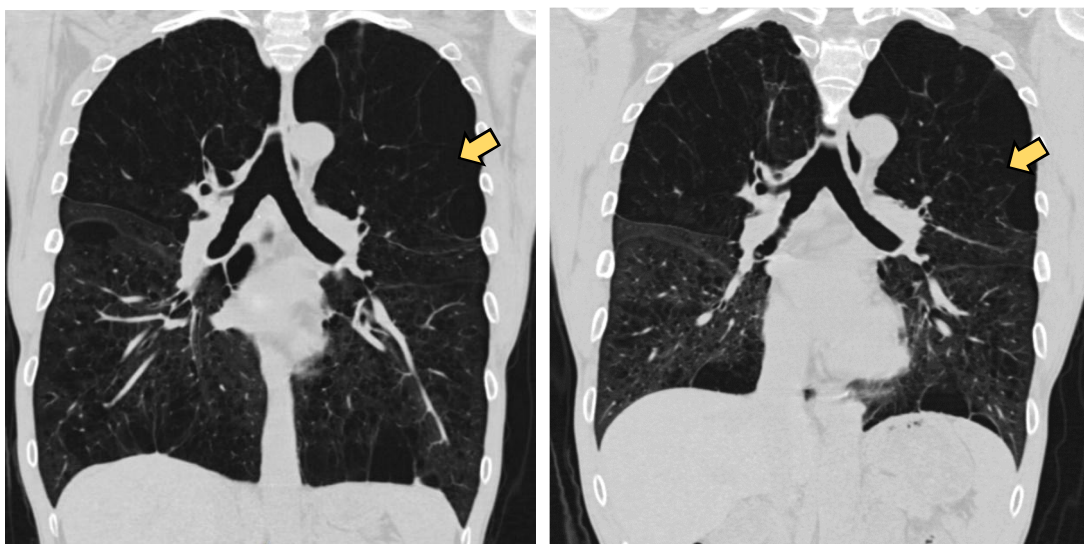
In the case of COPD, the lung alveoli wall degrades as the remodeling proceeds, thus became more compliant and transferred the mechanical stress into a strain more directly. So both volumetric portion and the total amount of deformation are analyzed with the term AAVC(%) and EVM, respectively. However, in the case of IPF, the fibrotic remodeling of parenchyma makes the local tissues stiffer, resulting in the total amount of the lung deformation tends to be decreased drastically with the shortness of breath. Then the passive motion driven by the motion of the chest wall cannot transfer the negative pressure into the deformation. Thus, the total amount of deformation has less implication than in the COPD. Thus, this study used only the volumetric changes as the term of AAVC(%) for the analysis of the deformation in IPF patients.

3. Application to diseases

3-1. Chronic Obstructive Pulmonary Disease (COPD)

(Disease Characteristics) COPD is a chronic pulmonary disease that causes airflow obstruction at the lungs. Typical symptoms are productive cough, shortness of breath ⁵¹. Emphysema on lung parenchyma and chronic bronchiolitis on the lining of the bronchial tubes are two major aspects contributes to COPD.

Figure 13. showed the emphysematous area in inspiratory and expiratory CT scan of severe COPD patients. Long-term exposure to irritants, including tobacco smoke, dust, chemicals, fumes from burning fuels, genetics, causes an inflammatory response in the lungs, resulting in abnormal remodeling of the tissues followed by narrowing of the small airways and breakdown of lung parenchymal tissue ⁵².



(a)

(b)

Figure 13. Emphysematous area (arrow-line) in inspiratory(a), and expiratory(b) CT Image of severe COPD patient (FEV1% =24%)

In chronic obstructive pulmonary disease (COPD) prognosis, the underlying morphologic abnormalities in the airways and alveoli underlie the heterogeneity of clinical outcomes and mortality⁵³. Long-term prospective studies in various settings have succeeded in identifying significant prognostic markers^{54, 55}. Specifically, in quantitative imaging, Haruna et al.⁵⁶ showed that the percentage of a low attenuation area (LAA) on chest computed tomography (CT) effectively predicts mortality. In contrast, although there is an association between CT airway measurements and COPD risk⁵⁷, the relationship with mortality remains unclear. Advanced quantitative imaging technologies have yet to be used to strengthen prognosis. I propose implementing the physical properties, including deformation and morphometric complexity in CT images of COPD patients to improve survival prediction.

3-1-1. Materials

3-1-1-1. Subject and Dataset – KOLD Cohort

(Patients and clinical assessments) Written informed consent was obtained from all patients. Records of subjects from a Korean obstructive lung disease (KOLD) cohort were retrospectively reviewed. All subjects met the following criteria: a diagnosis of COPD, i.e., post- BD forced expiratory volume in 1 s (FEV1)/forced vital capacity (FVC), 0.7, and no or minimal abnormality, other than emphysema, on chest radiographs. The KOLD study design has been published previously⁵⁸. COPD patients who underwent baseline CT scans between June 2005 to June 2015, and also underwent 3rd-year follow-up CT scans were enrolled. The CT scan includes 2 volumes for a patient – images at inspiration and at expiration.

And their survival status in February 2017 was ascertained. Age, sex, and smoking history were recorded, and body mass index, 6-min walking distance, and dyspnoea scale were measured at enrolment. For all patients, all test results, measurements, spirometry testing, and CT scans were acquired within 1 month of enrolment. Pulmonary function tests and CT scans were performed according to the KOLD cohort study protocol⁵⁸. The BODE index was calculated in accordance with Celli et al.⁵⁴. Table 3. presents the baseline and 3rd year follow-up characteristics of consorted COPD patients.

Table 3. Baseline and 3rd-year follow-up characteristics of 60 COPD patients

Characteristics	At enrollment Median (range)	In 3rd year Median (range)
Age (years)	65 (45–78)	-
Sex (Male:Female)	57:3	-
Pack-year ^a	43 (12–108)	-
BMI	23 (17–32)	23 (15–32)
6MWD ^b (m)	472 (145–598)	459 (80–605), 3 missed
SGRQ score ^c	32 (0–71)	28 (3–84)
Dyspnea scale ^d	2 (0–4)	2 (0–4)
FEV1% predicted ^e	50 (20–84)	54 (20–87), 1 missed
GOLD stage ^f	I (mild): 8 II (moderate): 22 III (severe): 25 IV (very severe): 5	I (mild): 10 II (moderate): 27 III (severe): 18 IV (very severe): 4 Missed: 1
cDLCO% predicted ^g	75 (23–144)	67 (12–125), 3 missed

^a Pack-year = the number of packs of cigarettes smoked per day multiplied by the number of years the person has smoked

^b 6-minute walk distance = distance walked by patients for 6 minutes

^c SGRQ score = Saint George's Respiratory Questionnaire total score

^d Dyspnea scale = modified Medical Research Council scale that stratifies the severity of dyspnea in respiratory diseases

^e FEV1% predicted = Forced expiratory volume in 1 Second, adjusted by the normal predictive values of spirometry in Korean population ⁵⁹.

^f GOLD stage = The Global Initiative for Chronic Obstructive Lung Disease stage

^g cDLCO% = the percentage of diffusing capacity of the lung for carbon monoxide corrected with hemoglobin to the expected value

(CT acquisition) Patients were scanned by Somatom Sensation (Siemens Medical Systems, Erlangen, Germany) using a 0.75 mm collimation, 100 eff. mAs, 140 kVp, and pitch 1.0. The scale of attenuation coefficients in the CT scanner ranged from -1024 to 3072 Hounsfield units (HU). Patients were scanned at full-inspiration and cranio-caudally while in the supine position and without contrast medium. The effective dose of the CT protocol was ~11 mSv. The CT images were reconstructed to 512 × 512-pixel Digital Imaging and Communications in Medicine format using the soft reconstruction kernel (B30f; Siemens Medical Systems)

(Ethics Statement) This study was approved by the institutional review board of the Asan Medical Center (no. 2005-0345). And each patient provided written informed consent. The study subjects were selected from the Korean Obstructive Lung Disease (KOLD) cohort.

3-1-1-2. Image-based physical Biomarkers

(Emphysema index) EI is calculated from the CT scan of inspiration, as the percentage of low-attenuation area in the lung. The Threshold of the low-attenuation area is under -950 in Hounsfield Unit (HU), which represents ‘almost vacant’ spaces formed as cumulated results of abnormal remodeling. EI is known to have a significant association with the mortality of the COPD patients⁶⁰, thus compared to other proposed biomarkers in this study. Based on the CT scan, emphysematous lesion masks (voxels in less than -950 HU in the lung) and lung parenchyma masks (voxels in between -950 HU and -400 HU) were computationally identified. EI%_s (the percentage of the lung volume occupied by emphysema) was calculated by dividing the emphysematous lesion volume by the whole lung volume of the same CT dataset.

(Measures about deformation – AAVC%) On the other hand, volumetric change was critical in the function of lung and heart, as the cardiac blood flow happens as much as the volume change of the endocardial surface, and airflow happens as much as the volume changes of the parenchymal wall. Thus, volumetric changes described in the previous section were used for this study. In the case of lung analysis, it is defined as Average Air Volume Change (AAVC%), an averaged global value throughout the region of interest for every case.

(Measures about deformation – EVM) Equivalent strain via Von-Mises (EVM) criterion is used as of the representative amount of the deformation, including deviatoric shearing and longitudinal stretching. With the same convention to the AAVC%, it is defined as an averaged global value throughout the region of interest for every case.

3-1-1-3. Clinical Measures

(Spirometry) FEV1% and cDLCO% were selected among the spirometry measures as representatives of ventilation and diffusion capacity performance, respectively. Post-bronchodilator administration forced expiratory volume in one second was measured by spirometry, and FEV1% predicted was estimated according to Korean formula [최정근]. Diffusion capacity for carbon monoxide measurement was performed, corrected with hemoglobin, and cDLCO% predicted was estimated by 전남대 formula. For both FEV1% and cDLCO%, 100% indicates the patient exhibiting standard ventilatory and diffusion capacity. Lower FEV1% and cDLCO% are hallmarks of severer COPD: lower FEV1% indicates severer airflow limitation and severer airway remodeling, whereas lower cDLCO% indicates low diffusion capacity and severer emphysema.

(Patient Characteristics) Age, BMI, pack-year of COPD patients were selected among the patient characteristics. Age is one of the criteria of COPD diagnosis, and BMI showed a high association on the survival of COPD patient⁵². As a measure of smoking history, pack-year was selected. Pack-year is the number of packs of cigarettes smoked per day multiplied by the number of years the person, reporting the cumulative exposure to one of the major irritants, tobacco smoke. These three measures were selected as the clinical measures from patient characteristics to be compared to other proposed physical biomarkers in this study.

(Quality of Life measures) The Saint George's Respiratory Questionnaire (SGRQ) is a questionnaire that measures the quality of life in patients with diseases of airways obstruction, comprised of three domains: symptoms, activity, and psycho-social. The total score was used in the current study. The total score range 0–100, higher scores indicating more limitations in the patient's quality of life. Distance walked by patients for 6 minutes (6MWD) was tested for the enrolled COPD patients following the ATS/ERS guidelines. The 6MWD test is a sub-maximal exercise test that assesses aerobic capacity and endurance. There is no upper bound for 6MWD. A longer 6MWD implies better exercise capacity of a patient. To quantify the severity of dyspnea a modified Medical Research Council dyspnea scale was investigated for enrolled patients. Dyspnea scale stratifies the severity of dyspnea in respiratory diseases from 0 to 4. The higher the dyspnea scale, the severer the symptom is.

3-1-2. Results & Discussions

(Correlation with Clinical Measures) Spearman's correlation between image-based physical biomarkers and clinical measures were analyzed to investigate whether the respiratory deformations could quantitatively assess the pulmonary function. As the irreversible nature of pathophysiology and asymmetric patient characteristics (age, sex etc.), correlation methods assuming the standard distribution of the sample set, for example, Pearson's, were considered to be inappropriate for the statistical analysis of COPD.

As a cross-sectional analysis, baseline physical biomarkers are compared with baseline clinical measures to identify propounding associations, and also between 3rd-year follow-ups.

As a prognostic analysis, baseline physical biomarkers were compared with 3rd-year follow-up clinical measures, with changes from baseline to 3rd-year follow-up clinical measures, respectively, to identify propounding associations. The relevant physical biomarkers were selected to be used in the regression study as followed.

(Regression of Lung Function Decline) FEV1% changes from baseline to third were considered to represent lung ventilation function decline of COPD patients⁵⁴, and multilinear regression model for FEV1% change was conducted by using the selected physical biomarkers along with known clinical measures, to investigate potentials of proposed biomarkers as independent contributions.

(Mortality & Acute Exacerbation) All target subjects were stratified into two groups having high- or low- valued physical biomarkers for the Kaplan-Meier survival analysis. All cause of death and acute exacerbation were analyzed, respectively.

(Prognosis in 6 years) In addition to mortality and acute exacerbation as clinical endpoints, a significant drop in FEV1%, 6MWD, and increase in dyspnea scale indicating COPD worsening in 6 years from the first visit are enrolled for clinical endpoints. Because there was no predetermined quantitative definition of "worsening" in FEV1%, 6MWD, and dyspnea scale, 6-year prognosis was dichotomously coded as follows:

(FEV1% event = 1) if FEV1% decreased more than 10% or died withing 6 years

(FEV1% event = 0) if the patient survived after 6 years and did not undergo more than 10% decrease in FEV1%

(FEV1% event = blank) if the patient were followed-up for less than 6 years, or missed spirometry

(6MWD event = 1) if 6MWD decreased more than 50m or died withing 6 years

(6MWD event = 0) if the patient survived after 6 years and did not undergo more than 50m decrease in 6MWD

(6MWD event = blank) if the patient were followed-up for less than 6 years, or missed the test

(Dyspnea event = 1) if dyspnea scale increased more than 1 level or died withing 6 years

(Dyspnea event = 0) if the patient survived after 6 years and did not undergo more than 1 level increase in dyspnea scale

(Dyspnea event = blank) if the patient were followed-up for less than 6 years, or missed interview

Logistic regressions were performed to find out associations between the physical biomarkers and the 6-year prognosis of FEV1%, 6MWD, and dyspnea scale.

(Tools of Statistical analysis) R statistics software version 3.6.3 (R Foundation for Statistical Computing, Vienna, Austria) and the following R packages were used for statistical analysis: SurvivalROC [Patrick J. Heagerty and packaging by Paramita Saha-Chaudhuri (2013). survivalROC: Time-dependent ROC curve estimation from censored survival data]; survival⁶¹; survminer⁶²; ggplot2⁶³.

3-1-2-1. Correlation with Clinical Measures

Table 4. Physical biomarkers in baseline and 3rd year follow-up of 60 COPD patients

Characteristics	At enrollment Median (range)	In 3rd year Median (range)
AAVC% ^a	-39% (-65% ~ -12%)	-43% (-74% ~ -10%)
EVM ^b	1.07 (0.82 ~ 2.31)	1.13 (0.76 ~ 1.90)
Emphysema Index % ^c	23 (2–58)	25 (2–67)

^a AAVC% (Average air volume change %) = average of the pixel-wise volumetric deformation in a patient, between inspiratory and expiratory moment, for the whole lung parenchymal area

^b EVM (Equivalent Von-Mises Strain) = average of the pixel-wise equivalent deformation in a patient, between inspiratory and expiratory moment, for the whole lung parenchymal area. Deviatoric and volumetric deformations be combined to build equivalent strain.

^c Emphysema Index % = the percentage of the lung volume occupied by emphysema

(Baseline Physical Biomarkers to Baseline Clinical Measures) Table 5 showed the correlation matrix between image-based physical biomarkers and clinical measures both in the baseline.

6MWD and SGRQ score showed better association with AAVC% than others, which implies dynamic volume changes are more closely related to exercise capacity and quality of life on COPD patients, than measures directly calculated from the CT attenuation (Emphysema Index%) or the cumulative amount of physical deformations combining all deviatoric and volumetric components (EVM).

FEV1% also showed better association with AAVC% than others, however only subtle differences occurred between 4 image-based biomarkers. This implies that the pulmonary ventilation function can be explained either via static-morphological or dynamic-deformational aspects of lung physics.

cDLCO%, diffusion capacity showed a strong association with Emphysema Index% that reflects changes in the area of intact gas exchange surface.

Among patient's characteristics, age and pack-year showed null associations with all 4 imaging biomarkers. On the other hand, BMI showed associations with all 4 imaging biomarkers, and association with EVM was relatively stronger than others, whereas the association with AAVC% was less than half of that with EVM. Considering the nature of the EVM as the cumulative physical deformation combining deviatoric and volumetric directions, deviatoric deformation may dominate the association with BMI. Patients with higher BMI requires higher metabolic demand, and easily experience shortness of breath than lean (lower BMI) people. Though further study is required to validate this conjecture, deviatoric deformation may represent a mismatch between metabolic demands and gas exchange performances in COPD patients.

On the other hand, no significant associations were found among AAVC%, EVM, EI% and smoking history, and patients' age (data not shown).

Table 5. Associations by Spearman's correlation coefficients (ρ) between physical biomarkers (AAVC%, EVM, Emphysema Index%) in baseline and clinical measures (6MWD, SGRQ score, FEV1%, cDLCO%, BMI, Dyspnea scale)

Character- istics	Spearman's correlation coefficients (ρ)					
	6MWD (m)	SGRQ score	FEV1%	cDLCO %	BMI	Dyspnea scale
AAVC%	0.34	-0.46	0.55	-	-	-0.35
EVM	-	-	0.42	0.22	0.53	-
Emphysema Index%	-0.25	0.34	-0.45	-0.77	-0.42	-

(Baseline Physical Biomarkers to 3rd year Follow-up Clinical Measures) Table 6 shows the correlation matrix between image-based physical biomarkers in baseline and clinical measures in 3rd-year follow-up. Interestingly, Emphysema Index% significantly associated with the dyspnea scale of the 3rd whereas there was null associations at the baseline.

Table 6. Associations by Spearman’s correlation coefficients (ρ) between physical biomarkers (AAVC%, EVM, Emphysema Index%) in baseline and clinical measures (6MWD, SGRQ score, FEV1%, cDLCO%, BMI, Dyspnea scale) in 3rd year follow-up.

Character- istics	Spearman’s correlation coefficients (ρ)					
	6MWD (m)	SGRQ score	FEV1% %	cDLCO %	BMI	Dyspnea scale
AAVC%	0.46	-0.43	0.48	-	0.32	-0.27
EVM			0.40	-	0.52	-
Emphysema Index%	-0.27	0.40	-0.44	-0.80	-0.45	0.51

(Baseline Physical Biomarkers to baseline-3rd year changes in Clinical Measures)

Table 7 showed a correlation matrix between image-based physical biomarkers in baseline and changes of clinical measures from baseline to 3rd-year follow-up. AAVC% significantly associated with Δ 6MWD in three years, and Emphysema Index% and Df significantly associated with Δ BMI and Δ Dyspnea scale in three years. No other significant associations were found.

Table 7. Associations by Spearman’s correlation coefficients (ρ) between physical biomarkers (AAVC%, EVM, Emphysema Index%) in baseline and three-year changes in clinical measures (Δ 6MWD, Δ SGRQ score, Δ FEV1%, Δ cDLCO%, Δ BMI, Δ Dyspnea scale).

Character- istics	Spearman’s correlation coefficients (ρ)					
	Δ 6MWD (m)	Δ SGRQ score	Δ FEV1 %	Δ cDLCO %	Δ BMI	Δ Dyspnea scale

AAVC%	0.26	-	-	-	-	-
EVM	-	-	-	-	-	-
Emphysema Index%	-	-	-	-	-0.30	0.38

(Regression of Lung Function Decline) A multivariable linear regression model was built to predict the extent of lung function decline designated by the three-year change of FEV1% predicted with physical biomarkers and clinical measures as predictors. All candidate predictors failed to predict the three-year change of FEV1% predicted except Emphysema Index%. As a whole, the adjusted R² of the linear regression model to predict Δ FEV1% in three years as small as 0.06, implying that the prediction power of the model is very limited.

Table 8. Parameters estimated by a multivariable linear regression model for Δ FEV1% as dependent variable and AAVC%, EVM, Emphysema Index%, Pack-year, age, BMI, Dyspnea scale, 6-minute walk distance, and SGRQ score as independent variables

Dependent var. Parameters	Δ FEV1%, adjusted R ² = 0.06	
	β coefficient	P- value
AAVC%	11.74	0.26
EVM	0.40	0.97
Emphysema Index%	-0.17	0.02
Pack-year	0.01	0.74
Age (years)	0.19	0.13
BMI	-0.36	0.32
Dyspnea scale	2.20	0.07
6-minute walk distance	0.00	0.91
SGRQ score	0.02	0.80

(Limitation of the Study) A major limitation of the current study is little change of lung function in three years of follow-up. In Table 3 shows the characteristics of the subjects, only subtle changes in lung function measures including FEV1% took place in three years, undermining the initial goal of the study to observe the progressing pathophysiology through a window of physical property analysis. The more-than-expected stability of the COPD patients could be caused by medical interventions, or otherwise, the nature of the disease. Taking a longer follow-up period or restricting medical interventions could be potential solutions, but these are not realistic nor ethical at the current point.

3-1-2-2. Mortality & Acute Exacerbation

(Mortality) Figure 14 showed Kaplan-Meier survival analysis for all cause of death with the stratified AAVC% and EVM. Because there is no apparent threshold for these markers, subjects were stratified into two strata at the median. Patients with higher AAVC%, and higher EVM seem to survive longer, but not significantly by 95% confidence interval for all time (overlapping shade).

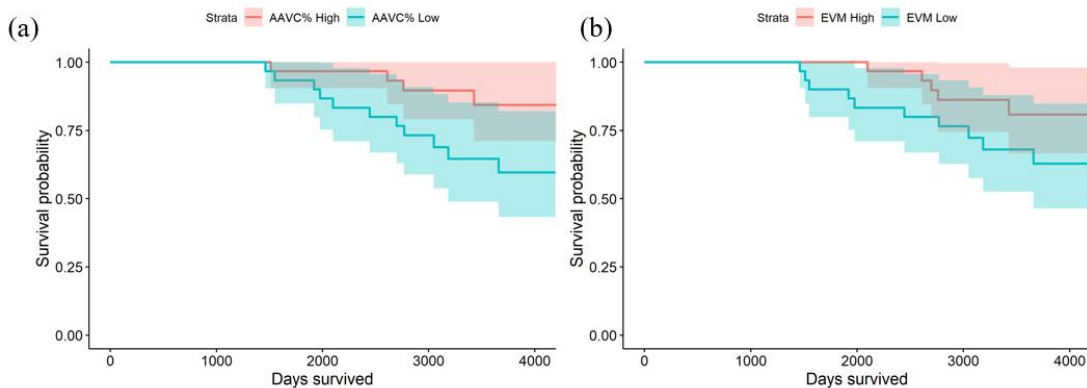


Figure 144. Survival curves for high- and low- strata stratified by (a) AAVC% and (b) EVM. 95% confidence interval is shown in shades.

(Acute Exacerbation) Figure 15 showed Kaplan-Meier survival analysis for acute exacerbation with the stratified AAVC%, EVM. Subjects were stratified into two strata at

median as in survival analysis. Patients with lower AAVC% seem to survive longer, but not significantly by 95% confidence interval for all time (overlapping shade).

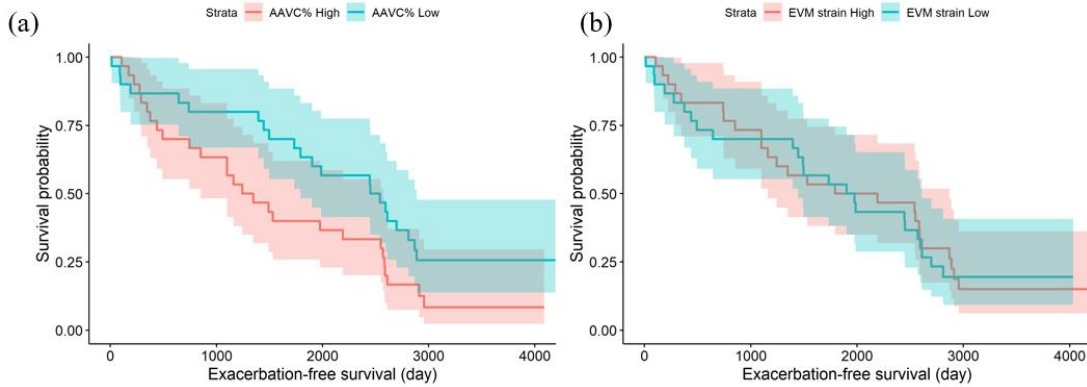


Figure 155. Exacerbation-free survival curves for high- and low- strata stratified by (a) AAVC%, and (b) EVM. 95% confidence interval is shown in shades.

3-1-2-3. Prognosis in 6 years

The associations between AAVC%, EVM, and 6-year prognosis of FEV1% drop, 6MWD drop, and dyspnea scale increase are shown in table 9. Smaller EVM was significantly associated with the chance of more the 10% drop in FEV1% or death within 6 years, but no other significant associations were found.

Table 9. Association between AAVC%, EVM and 6-year prognosis of FEV1%, 6MWD, and dyspnea scale.

Clinical endpoints	β coefficient (95% Confidence Interval)	
	AAVC%	EVM
FEV1% ^a	3.16 (-2.23–9.00)	-5.57 (-11.65–0.39)
6MWD ^b	2.79 (-2.41–8.34)	-2.19 (-6.70–2.10)
Dyspnea scale ^c	-1.58 (-6.40–3.04)	-1.25 (-5.67–3.01)

^a FEV1%: More than 10% drop in FEV1% predicted or death within 6 years. FEV1%, forced

expiratory volume in 1 Second, adjusted by the normal predictive values of spirometry in Korean population.

^b 6MWD = More than 50m drop in 6MWD or death within 6 years. 6MWD, distance walked by patients for 6 minutes

^c Dyspnea scale = More than 1 level increase in dyspnea scale or death within 6 years. Dyspnea scale, modified Medical Research Council scale that stratifies severity of dyspnea in respiratory diseases

(Implications sum-up) New imaging biomarkers representing physical aspects of the lung are suggested; AAVC%, EVM, Df – representing the aspect of the volumetric subtotal of deformation tensor, equivalent amount of deformation at a point as a scalar(direction-less).

Then the physical biomarkers are compared with a conventional imaging biomarker, Emphysema Index%, in relation to lung functions, exercise capacity, diffusion capacity, dyspnea scale, mortality, and acute exacerbation.

AAVC% at enrollment significantly associated with 6MWD, SGRQ, FEV1%, and Dyspnea scale at enrollment, 6MWD, SGRQ, FEV1%, BMI, and Dyspnea scale in 3rd-year follow-up, and 6MWD change in three years. Higher AAVC% indicated less severe pathology. AAVC% failed in predicting three-year decline of FEV1%. In survival analysis, patients with higher AAVC% survived better than patients with lower AAVC% in all-cause-of-death, and the opposite in exacerbation, but not significantly in both.

EVM significantly associated with FEV1%, cDLCO%, and BMI at enrollment, FEV1%, and BMI in the 3rd year of follow-up, and none of the three-year changes. Similar to AAVC%, higher EVM indicated less severe pathology and also failed in predicting three-year decline of FEV1% and survived better but not significantly. EVM failed in predicting exacerbation but showed a negative association with FEV1% prognosis in 6 years.

(Discussion) COPD is a very heterogeneous disease, and the definition and understanding of the disease are ever-evolving^{64,65}. In previous studies, it has been quite common to find out paradoxical or contradictory observations in spirometry, CT analysis, patient-reported symptoms, and prognosis. Martinez et al. stated that the heterogeneity of COPD comes from the variability of disease trajectories, so single modality alone are not enough to understand the pathophysiology of COPD, whether it is CT or spirometry^{64,65}. Indeed, a randomized controlled trial for home spirometry telemonitoring usage failed to show a significant prediction power for COPD exacerbation, implying that FEV1 is not always prognostic⁶⁶. Respiratory symptoms and the patient-reported quality of life measures are not always concordant with other COPD biomarkers either and are subjective⁶⁷. There are patients with normal CT features but with severe airflow limitation⁶⁸, whereas other patients have emphysematous CT findings but with normal spirometry⁶⁹. Also, there are “PRISm” (Preserved Ratio Impaired Spirometry) patients who have $FEV1/FVC > 0.7$ but have $FEV1\% < 80\%$, those patients are not in GOLD criteria but have higher risks of mortality than healthy population⁷⁰. Moreover, an unstable definition of exacerbation⁷¹ adds additional heterogeneity in understanding the pathophysiology of COPD.

AAVC% and EVM have their unique physical implication and are independent of the pre-existing COPD biomarkers. The physical biomarkers may shed new light on the complex and changing landscape⁶⁵ of COPD, although they alone did not show reliable prognostic power. For example, AAVC% and EVM may be utilized in newly defining COPD endotypes in paradoxical cases such as PRISm patients or patients with discordant spirometry and CT findings. For example, in normal-looking chest CT of smokers, Bodduluri et al. revealed there were air trapping by performing inspiration-expiration CT registration⁷². Applying the suggested physical analysis may also find out signs of abnormality in the lung. Also, AAVC% and EVM may be assorted together with the pre-existing COPD biomarkers to be fed to a deep learning model for disease staging and prognosis⁷³ as additional imaging features.

3-2. Idiopathic Pulmonary Fibrosis

(Disease Characteristics) Idiopathic pulmonary fibrosis is a chronic lung disease characterized by a progressive and irreversible decline in lung function⁷⁴. Typical symptoms are cough and gradual onset of shortness of breath and diagnosed with the presence of a typical radiological pattern of usual interstitial pneumonia (UIP) on high-resolution computed tomography.

Figure 16. showed UIP patterns in inspiratory and expiratory CT scan of severe IPF patients. The cause of IPF is unknown; however, certain environmental factors and exposures have been shown to increase the risk of getting IPF⁷⁵. Long-term exposure to irritants, including tobacco smoke, dust, silica, occupations related to farm, have also been shown to increase the risk for IPF⁷⁵.

Quantitative CT analysis has been proved its prognostic power in IPF, including mortality and FVC decline as clinical endpoints⁷⁶⁻⁷⁹. However, Fukihara et al.⁸⁰ reported a null association between CT pattern and survival and exacerbation, stating that IPF has much to be studied further, and CT physical analysis has not been performed for IPF patients before.

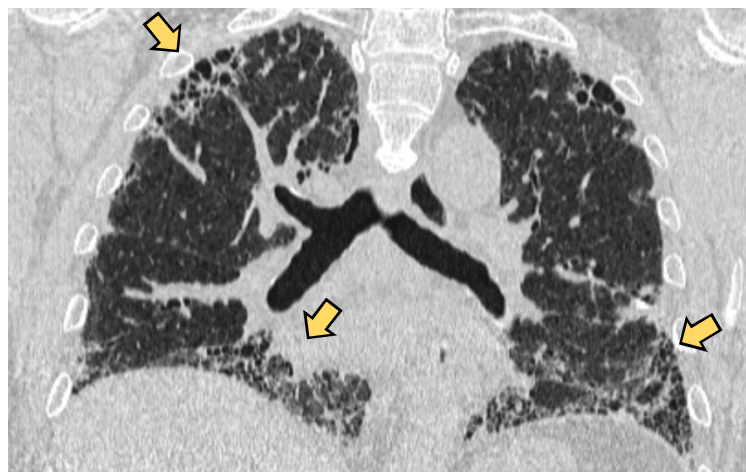


Figure 16. UIP patterns (arrow-line) in inspiratory CT Image of IPF patient (FVC% =41%)

3-2-1. Materials

3-2-1-1. Subjects and Dataset

(Patients and clinical assessments) Patients who diagnosed as UIP in Asan Medical Center from June 2016 to February 2017 were retrospectively reviewed. All subjects met the following criteria: a diagnosis of IPF via biopsy and cross-validated via UIP patterns in CT. The CT scan includes 2 volumes for a patient – images at inspiration and at expiration. For all patients, all test results, measurements, spirometry testing were acquired within 3 months of CT scans date. Pulmonary function tests and CT scans were performed according to the KOLD cohort study protocol ⁵⁸. Table 10 presents the Demographics of 30 Patients reviewed.

Table 10. Demographics of 30 IPF Patients

Categories	Characteristics	At enrollment Mean ± SD
Patient Characteristics	Age (years)	68.3 ± 5.1
	Sex (Male:Female)	27:3
	Center / Nation	Asan Medical Center / Rep. of Korea
Diagnosed Criteria	CT	UPI Patterns identified
	Biopsy	472 (145–598)
PFT	FVC (Mandatory)	70.0 ± 16.9

3-2-1-2. Image-based physical Biomarkers

(Measures about deformation) AAVC% was considered to be critical for this disease as the disease progress changes more tissues into fibrotic cells – implying that lung parenchyma will become stiffer and gas exchange performance is expected to decrease with it. Thus, following the restrictive character of IPF, AAVC% for the whole lung was selected as the primary measure. And a stratification was additionally applied to the AAVC%, so in 4 high attenuation areas (HAAs) augmented by the HAAs' volume fraction, were investigate to check the effect of the regional fibrosis (Figure 17). The lower thresholds for HAAs were selected from -900 to -600 in HU by the step of 100 HU, to access fibrosis-rich proportion of lung.

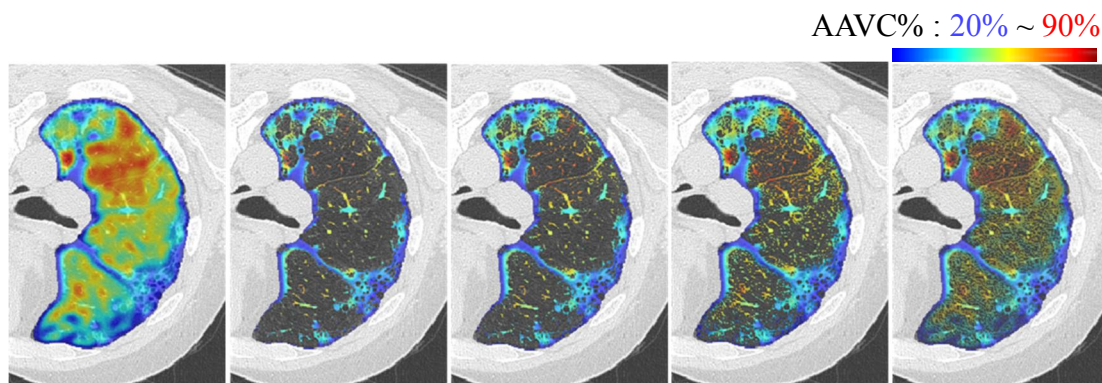


Figure 17. AAVC% of whole lung and HAA augmented AAVC% over -600, -700, -800, -900 in (HU), during expiration.

3-2-1-3. Clinical Measures

(Spirometry) Forced vital capacity (FVC) has been used for decades to assess and describe the functional status of patients with fibrotic lung diseases; a decline of FVC was utilized as a measure of disease progression⁸¹. Also, studies have demonstrated that a 10% decline in forced vital capacity (FVC) within 6 to 12 months was associated with a significant increase in mortality^{82, 83}.

3-2-2. Results & Discussions

(Correlation with Clinical Measures) Pearson's correlation between image-based physical biomarkers and clinical measures were analyzed to investigate whether the respiratory deformations can quantitatively assess the pulmonary function. As a cross-sectional analysis, HAA augmented AAVC% are compared with baseline FVC% to identify associations.

(Tools of Statistical analysis) R statistics software version 3.6.3 (R Foundation for Statistical Computing, Vienna, Austria) and the following R packages were used for statistical analysis; ggplot2 ⁶³.

(HAA augmented AAVC to FVC%) Table 11 showed a significant correlation between HAA augmented AAVC to FVC%. AAVC at HAA over -600 HU showed better correlation with FVC, than AAVC in the whole lung. High attenuation area (HAA) signifies the fibrotic region; thus, HAA cut can be one way of augmentation for AAVC measure for pulmonary function in IPF patients. HAA threshold -600 seems the best among the tried; however, the size of the statistical sample is marginal to suggest the use of threshold value.

Table 11. Associations by Pearson's correlation coefficients between 5 stratifies AAVC in HAA, and FVC%

AAVC%	Pearson's correlation coefficients with FVC%	
	Adjusted R ²	P value
in whole lung	0.411	< 0.001
in HAA (over -600 HU)	0.640	< 0.001
in HAA (over -700 HU)	0.600	< 0.001
in HAA (over -800 HU)	0.488	< 0.001
in HAA (over -900 HU)	-	-

3-3. Left Ventricle Contractility

(Note of referencing the published article) The research described below is composed by the extraction and rearrangement from the published article⁸⁴ of which mechanical frameworks were formulated and assessed by the thesis candidate.

(Deformation analysis from 3D Echocardiology) Recently, 3D strain analysis has been developed to overcome these limitations⁸⁵. More from the directional strains, the global principal strain (GP1S) is defined as the sum of local strains in principal directions where shear deformations are absent, and its physical and physiological implications have been studied^{86, 87}. Reconstruction of the functional strain using 3D echocardiography is a novel technology that enables an accurate assessment of 3D geometrical deformation of the LV surface⁸⁸. This information is not available from 2D echocardiography, which only displays cross-sectional images of an anatomical body from a fixed number of axes.

Although 3D GP1S seems to represent major direction and magnitude of ventricular contractility by its definition, it remains to be validated with invasive parameters for ventricular contractility. This study aimed to demonstrate directional characteristics of 3D strains reflecting LV endocardial contraction and to validate the 3D GP1S using gold standard invasive parameters representing LV systolic function in comparison with conventional strains, such as GLS and GCS.

3-3-1. Materials & Methods

3-3-1-1. Subjects and Dataset

(Animal test to control inotropic status) An animal experiment was performed (Beagles) to acquire both invasive cardiac measures as catheterized pressure-volume (PV) loop cycle and speck-tracked physical motion of myocardium from the 3D echocardiology simultaneously under different controlled inotropic statuses. All animal experiments were performed according to the protocols approved by the Institutional Committee for the Use and Care of Laboratory animals. The details description are in the published article⁸⁴.

3-3-1-2. Image-based physical Biomarkers

(Global strains from 3D echocardiography) Echocardiograms of the left ventricle were acquired from the apical four-chamber view [E9, 1.5–4.0 MHz four-dimensional (4D)-V transducer, GE Vingmed, Horten, Norway] simultaneously with PV loop acquisition. For each inotropic state, 3D images were collected with a frame rate ranging from 30 to 55 frames per second. Based on the established speckle-tracking method⁸⁹, endocardial wall motion was extracted in the form of four-dimensional point grids using the TomTec Imaging Systems (Unterschleissheim, Germany). Then, the triangular meshes were generated from the grid of dots (Figure. 18), which were assumed a reasonable approximation of LV endocardial surface at each time frame and they were used to compute strains.

(Omitted registration process) Tomtec, SW for 4D echocardiology ultrasound image analysis, automatically tracks down and provides the point-grid of endocardial surface to the researchers, thus the registration process defined in the former section omitted.

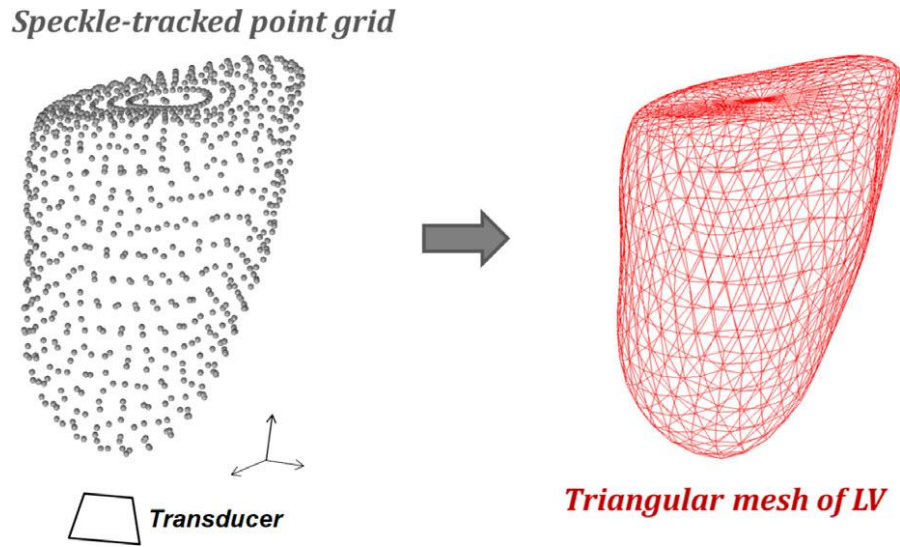


Figure 18. Generation of triangular mesh. In each time frame, grids of speckle-tracking points were obtained at the LV endocardial surface to analyze temporal motion of a curved surface in three-dimensional space.

(Categories of the Physical Biomarkers) The endocardial surface of the left ventricle was assumed smooth enough to be approximated by the Euclidean plane with a reasonable degree of accuracy. No abrupt or large-scale deformation appeared to be taking place either. Strains calculated on each mesh would locally approximate elasticity of the region where the mesh represents. With these hypotheses, global strains were formulated global strain as the arithmetic average of calculated local strains. For each mesh, general displacement field u relative to the position at end diastole was calculated. Polar decomposition of the measured motion was used to eliminate effects of rigid-body displacement and rotation and to extract pure deformation.

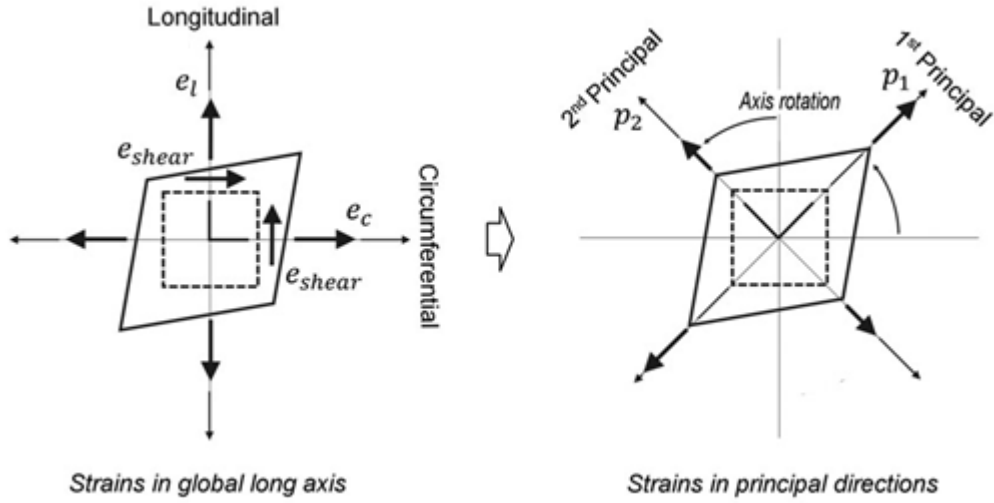


Figure 19. Principal analysis where in the concurrent coordinate having no shear deformations.

From the Lagrangian finite strain tensor E_{AB} calculated for each mesh, the strain components in global longitudinal direction, E_L , and global circumferential direction, E_C , were selected and averaged over the entire LV surface to obtain global longitudinal strain (GLS) and global circumferential strain (GCS), respectively. For each mesh, strain P_1 in the principal direction, a direction in which the effects of strain were maximized, was also computed and averaged over the LV endocardial surface to obtain main contractile global principal strain (GP1S). Secondary strain P_2 was calculated as an orthogonal effect of the principal direction and averaged into global secondary strains (GP2S).

$$\left[\begin{array}{ll} \text{GLS} = \frac{1}{n} \sum_{k=1}^n (E_L)|_{k \text{ th mesh}} & \text{GCS} = \frac{1}{n} \sum_{k=1}^n (E_C)|_{k \text{ th mesh}} \\ \text{GP1S} = \frac{1}{n} \sum_{k=1}^n (P_1)|_{k \text{ th mesh}} & \text{GP2S} = \frac{1}{n} \sum_{k=1}^n (P_2)|_{k \text{ th mesh}} \end{array} \right.$$

The aforementioned equations are the formulation of GLS, GCS, GP1S, and GP2S, where n denotes the number of meshes representing endocardial wall motion.

3-3-1-3. Clinical Measures

(Pressure–volume measurements with the control of inotropic states) The hemodynamic parameters, such as dp/dt max, and end-systolic pressure–volume relationship (ESPVR) were calculated. The details description are in the published article⁸⁴.

3-3-2. Results & Discussions

(Characteristics of LV Endocardial Strains) The direction of the 3D GP1S was apparently continuous, implying that speckle tracking and the strain calculation scheme captured major contractile behavior of the left ventricle (Figure 20(a)). Interestingly, GP1S line patterns in the endocardium appeared to be circumferential rather than longitudinal, while GP2S line patterns seemed to be longitudinal (Figure 20(b) and 20(c)). Considering that the strain can be decomposed either into longitudinal or circumferential directions or into principal or secondary directions, the LV endocardial wall of tested beagles showed dominant contraction in a circumferential direction. The temporal changes of global strains in a single cardiac cycle also showed that the GCS was a major component of deformation compared with GLS, and the difference was more obvious when the same deformation was expressed in GP1S and GP2S (Figure 20 (b) and (c)).

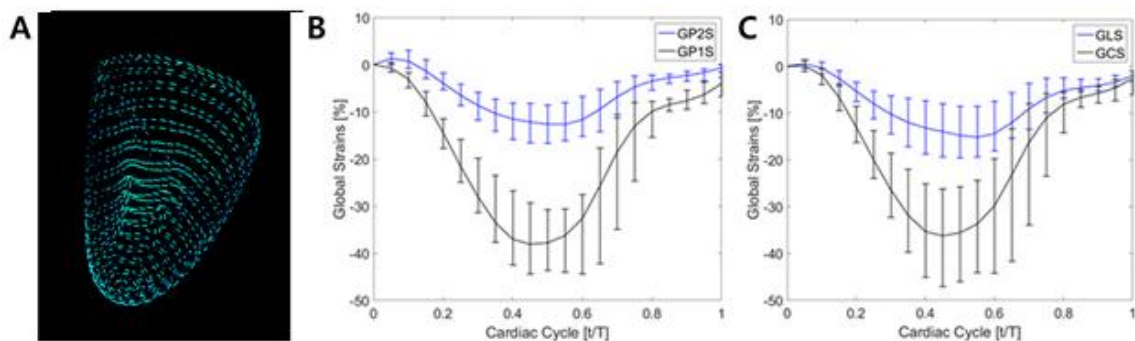


Figure 20. Three-dimensional principal strain line patterns of the left ventricular endocardium; (a) Representative vector map of principal strains at mid-systole. (b,c) Time evolution of the global strains obtained from 14 dogs at the baseline state: (b) principal (GP1S) and secondary (GP2S) strains, and (c) longitudinal (GLS) and circumferential (GCS) strains. The values are presented as mean \pm standard deviation using error bars.

(Relationship between 3D Strains and Invasive Measures) The strain data were compared with the invasive measurements from PV loop analyses through Pearson's correlation (Table 12). The GP1S and GP2S showed significant correlation with dP/dt and ESPVR. The dP/dt showed the best correlation with GP1S ($r=-0.845$, $p<0.001$), and ESPVR showed the best correlation with GP2S ($r=-0.819$, $p<0.001$). The GCS and GLS tended to correlate weaker with invasive measurements in comparison with GP1S and GP2S, respectively (Table 13).

Table 12. Associations by Pearson's correlation on the three-dimensional echocardiographic global strains and left ventricular systolic functions measured by catheterization

3D global strains (%)	LV systolic functions measured by catheterization			
	dP/dt max (mmHg/s)		ESPVR (mmHg/mL)	
	r	p-value	r	p-value
GP1S	-0.845	<0.001	-0.812	<0.001
GCS	-0.825	<0.001	-0.785	<0.001

GP2S	-0.842	<0.001	-0.819	<0.001
GLS	-0.717	<0.001	-0.733	<0.001

LV = left ventricular, ESPVR = end-systolic pressure-volume relationship, 3D = three-dimensional, GP1S = global principal strain, GCS = global circumferential strain, GP2S = global secondary strain, GLS = global longitudinal strain.

(Contribution of LV Volume Change in LV Systolic Functions) LV ejection fraction (EF), which is defined as the stroke volume divided by the end-diastolic volume, showed excellent correlations with GP1S and GCS (GP1S~EF $r=-0.896$, $p<0.001$; GCS~EF $r=-0.896$, $p<0.001$), but the correlation coefficient with GP2S and GLS was relatively low (GP2S~EF $r=-0.874$, $p<0.001$; GLS~EF $r=-0.645$, $p<0.001$). Further investigation was conducted the effect of volumetric change by correcting the strains with LV residual volume ratio (RVR, end-systolic volume to end-diastolic volume) and comparing their correlation coefficients to the invasive parameters with original strains' correlations (Table 13). The correlations between invasive measurements and GP2S or GLS were considerably strengthened when strains were corrected by the RVR, whereas correlations between invasive measurements and GP1S or GCS were weakened.

Table 13. Association by Pearson's correlation on the left ventricular systolic functions measured by catheterization and three-dimensional global strains corrected by residual volume ratio

3D global strains corrected by residual volume ratio (%)	LV systolic functions measured by catheterization			
	dP/dt (mmHg/s)		ESPVR (mmHg/mL)	
	r	p-value	r	p-value
GP1S/RVR	-0.803	<0.001	-0.788	<0.001

GCS/RVR	-0.782	<0.001	-0.766	<0.001
GP2S/RVR	-0.868	<0.001	-0.874	<0.001
GLS/RVR	-0.873	<0.001	-0.892	<0.001

LV = left ventricular, ESPVR = end-systolic pressure-volume relationship, 3D = three-dimensional, GP1S = global principal strain, GCS = global circumferential strain, GP2S = global secondary strain, GLS = global longitudinal strain, RVR= residual volume ratio.

(Contribution) This was the first study designed to validate the 3D echocardiographic principal strains for the assessment of LV systolic function by use of the gold standard invasive measures. The main findings of this study can be summarized as follows.

1) The endocardial principal strain showed predominantly circumferential behavior that might be considered as the reflection of LV volume change.

2) Principal decomposition of the myocardial 3D strains represented LV systolic functions more accurately than directional strains along the longitudinal and circumferential axes.

3) Because RVR represents the volumetric contribution to the LV contractile functions, among the components of the endocardial LV deformation, GLS and GP2S can be considered as portions, which are less dependent on the LV volume change.

(Assessment of Endocardial LV Deformation by 3D Principal Strain Analysis) There have been inconsistent reports regarding the directions of endocardial GP1S in humans. Mangual et al. reported ⁹⁰ that the subepicardial layer maintains a mostly circumferential strain path, whereas the subendocardium has regions of longitudinal and circumferential shortening. On the contrary, Pedrizzetti et al. ⁹¹ demonstrated that about one-half of the endocardium (lateral, inferior, and septal) contracted along the epicardial (cross-fiber) left-handed helical

direction. The anterior walls, particularly near the LV base, contracted along the right-handed helical subendocardial direction. In this study, the main contractile principal strain of the LV endocardium were more circumferential rather than longitudinal, and this is in agreement with that found in another previous report ⁹². This controversy with regard to the direction of endocardial GP1S were unknown, but it may be attributed to the differences in echocardiographic machines, endocardial tracking methods, and mathematical algorithm extracting strain directions.

Nevertheless, the functional direction of contraction must not necessarily coincide with the anatomic direction of the fibers; the two entities are complementary and integrative, and the former reveals how the activation of the latter contributes to reduction of the cavity volume ⁹⁰. In this study, LV EF showed better correlations with GP1S and GCS rather than GP2S and GLS, and this result indicates that GP1S is circumferential and associated with LV cavity volume change. The endocardial GP1S can be circumferential, even though this is not the direction of subendocardial muscle fibers, because the visible functional strain lines are related to the capacity of elastic response of the endocardial surface to the high systolic LV pressure ⁹³. Although the GP1S direction found in our study was circumferential, directions of GP1S and GCS were not identical. Furthermore, principal decomposition of the myocardial 3D strains showed excellent correlations with invasive gold standard parameters of LV contractility, and these correlations tended to be stronger than those of directional strains along the longitudinal and circumferential axes. This result indicates that GP1S and GP2S may be used as good 3D parameters of LV contractility.

(LV Volume Change and LV Contractility) The global strains were corrected with RVR to eliminate the confounding effects of deformation that resulted from a passive consequence of volume change. Correlations of GP1S and GCS with invasive parameters were rather weakened when they were corrected by RVR. However, in contrast, correlations of GLS and

GP2S with invasive parameters were enhanced after correction. This indicated that longitudinal contraction may have less contribution to LV volume change; thus, it may be a specific component of LV contraction independent of LV volume change.

(Limitation of the Study) First, this study was performed in animal models, and 3D tracking of the echocardiographic image was not possible in some dogs that could not be included in this study. The 3D echocardiography in the current stage is limited by low temporal and spatial resolution. Consequently, accuracy of the triangular meshes extracted from the 3D images had to be limited by the echocardiographic image quality.

Second, the strain values were obtained only from the endocardium, and entire myocardial tracking was not possible because of the limitation of the Tomtec software. Myocardial speckle tracking using another software was unsuccessful in this animal model, probably because of substantial tracking failure of the dogs' small heart size. The analysis results cannot be extrapolated to the principal strains derived from myocardial tracking.

4. Implications from three applications

Heart and lung are organs in motion to sustain its function, providing air and blood flows in the body through lifetime. Utilizing noninvasive imaging modalities such as CT and ultrasound, series of methods to analyze the physical motion in the lung and the heart are established and demonstrated herein. Principles and concepts of continuum mechanics are adopted and translated for application to the lung and the heart. Following image registration, generalized expression of motion and strain tensor as deformation was expanded, and methodology to assess physical motion with volumetric changes, principal strain, and equivalent strain was suggested. Putative sources of bias were examined, and adequate size of smoothing kernel was proposed.

Then the developed methods were deployed to assess physical motion analysis in COPD, IPF, and left ventricular contractility cases.

In analysis of COPD, image-based physical biomarkers, AAVC% and EVM were defined, measured, and tested for correlation with lung function features and for prognostic power. Although their prognostic power was rather incremental than expected, they correlated with the conventional COPD biomarkers such as EI% and independently contributed in prognosis.

In analysis of IPF, extent of fibrotic lesion represented by HAA% associated with AAVC%. The suggested image-based physical biomarkers are different from, and independent of the conventional intensity-based image biomarkers and unveiling another layer of information.

In analysis of cardiomyopathy, 3D echocardiographic principal strains for the assessment of LV systolic function is validated by the use of the gold standard invasive measures. The

endocardial principal strain calculated from the suggested calculation showed predominant circumferential behavior, and principal decomposition of the myocardial 3D strains represented LV systolic functions more accurately than directional strains along the longitudinal and circumferential axes.

Motivation behind the proposed methodological framework is to utilize it to anneal the knowledge gaps between micro- and macroscale understanding. As one of the typical examples, spirometry measures such as forced expiratory volume in 1-second (FEV₁) and forced vital capacity (FVC) are used to analyze airway obstruction, however they are global measures of lung which cannot capture the structural heterogeneity in lung diseases such as COPD⁹⁴⁻⁹⁶. Thus, obstructions in the peripheral airways and early onset of lung stiffening are often difficult to detect⁹⁷; the local pathologic remodeling those lead to local hypoxia may not be detectable by the lung function analysis because local hypoxia could be compensated with localized vasoconstriction thereby not resulting in an impaired lung function at a whole lung⁹⁸.

Not only in understanding of COPD, but IPF, and left ventricular contractility have such knowledge gaps, so the imaged-based physical biomarkers developed herein could be widely applied to other respiratory or cardiac diseases. Also, how physical properties change in a normative growing and aging process is of great interest where suggested biomarkers could play a pivotal role.

5. Conclusion

In this thesis, imaging biomarkers reflecting pulmonary and cardiac motions were constituted based on the mathematical and physical frameworks of the continuum media based on the well-established image registration methods. The constituted framework can provide the status of motion for biomechanical media under 12 degrees of freedom as two subgroups: displacement and deformation. Considering the nature of the intrinsic motions in heart and lung, physical biomarkers are expected to provide more quantitative and qualitative contributions with the additional augmentation techniques (localization, value-based & proximity stratification, parametric combination).

Using the biomarkers evaluated, investigations on two pulmonary diseases with clinical data and one left ventricular contractility with animal experiment were performed to find out their utility as physical biomarkers. Proposed biomarkers showed considerable association with clinical measures or concordant with medical understanding in all 3 cases, although in most of the cases, proposed biomarkers did not surpass the pre-existing clinical measures in prognostic power.

(future works) The gradient-based calculation procedures, from the image registration formula to the finite deformation analysis of the body, have potential elements of bias as described. Thus, in each application, validation based on the characteristics of the imaging modality and of the length/velocity scale of the target biomechanical situation are recommended prior to the physiological analysis.

6. References

1. WHO. The Top 10 cause of death. *WHO Fact Sheets*. 2020.
2. Zaitsev M, Maclaren J and Herbst M. Motion artifacts in MRI: A complex problem with many partial solutions. *J Magn Reson Imaging*. 2015;42:887-901.
3. Kalisz K, Buethe J, Saboo SS, Abbara S, Halliburton S and Rajiah P. Artifacts at Cardiac CT: Physics and Solutions. *Radiographics*. 2016;36:2064-2083.
4. Scott AD, Keegan J and Firmin DN. Motion in cardiovascular MR imaging. *Radiology*. 2009;250:331-51.
5. Amano Y, Yanagisawa F, Tachi M, Asai K, Suzuki Y, Hashimoto H, Ishihara K and Kumita S. Three-dimensional Cardiac MR Imaging: Related Techniques and Clinical Applications. *Magn Reson Med Sci*. 2017;16:183-189.
6. Kwon SH and Gopal AS. 3D and 4D Ultrasound: Current Progress and Future Perspectives. *Curr Cardiovasc Imaging Rep*. 2017;10:43.
7. Liu J, Wang Y, Wen Z, Feng L, Lima APS, Mahadevan VS, Bolger A, Saloner D and Ordovas K. Extending Cardiac Functional Assessment with Respiratory-Resolved 3D Cine MRI. *Sci Rep*. 2019;9:11563.
8. Schittny JC. How high resolution 3-dimensional imaging changes our understanding of postnatal lung development. *Histochem Cell Biol*. 2018;150:677-691.
9. Bamberg F. Quantitative Imaging and Imaging Biomarkers: The Search for Generalizability in Radiology. *J Thorac Imaging*. 2018;33:69-70.
10. deSouza NM, Achten E, Alberich-Bayarri A, Bamberg F, Boellaard R, Clement O, Fournier L, Gallagher F, Golay X, Heussel CP, Jackson EF, Manniesing R, Mayerhofer ME, Neri E, O'Connor J, Oguz KK, Persson A, Smits M, van Beek EJR, Zech CJ and European Society of R. Validated imaging biomarkers as decision-making tools in clinical trials and routine practice: current status and recommendations from the EIBALL* subcommittee of the European Society of Radiology (ESR). *Insights Imaging*. 2019;10:87.
11. Guo F, Capaldi D, Kirby M, Sheikh K, Svenningsen S, McCormack DG, Fenster A, Parraga G and Canadian Respiratory Research N. Development of a pulmonary imaging biomarker pipeline for phenotyping of chronic lung disease. *J Med Imaging (Bellingham)*.

2018;5:026002.

12. O'Connor JP, Aboagye EO, Adams JE, Aerts HJ, Barrington SF, Beer AJ, Boellaard R, Bohndiek SE, Brady M, Brown G, Buckley DL, Chenevert TL, Clarke LP, Collette S, Cook GJ, deSouza NM, Dickson JC, Dive C, Evelhoch JL, Faivre-Finn C, Gallagher FA, Gilbert FJ, Gillies RJ, Goh V, Griffiths JR, Groves AM, Halligan S, Harris AL, Hawkes DJ, Hoekstra OS, Huang EP, Hutton BF, Jackson EF, Jayson GC, Jones A, Koh DM, Lacombe D, Lambin P, Lassau N, Leach MO, Lee TY, Leen EL, Lewis JS, Liu Y, Lythgoe MF, Manoharan P, Maxwell RJ, Miles KA, Morgan B, Morris S, Ng T, Padhani AR, Parker GJ, Partridge M, Pathak AP, Peet AC, Punwani S, Reynolds AR, Robinson SP, Shankar LK, Sharma RA, Soloviev D, Stroobants S, Sullivan DC, Taylor SA, Tofts PS, Tozer GM, van Herk M, Walker-Samuel S, Wason J, Williams KJ, Workman P, Yankeelov TE, Brindle KM, McShane LM, Jackson A and Waterton JC. Imaging biomarker roadmap for cancer studies. *Nat Rev Clin Oncol*. 2017;14:169-186.

13. Crosby LM and Waters CM. Epithelial repair mechanisms in the lung. *Am J Physiol Lung Cell Mol Physiol*. 2010;298:L715-31.

14. Suki B, Sato S, Parameswaran H, Szabari MV, Takahashi A and Bartolak-Suki E. Emphysema and mechanical stress-induced lung remodeling. *Physiology (Bethesda)*. 2013;28:404-13.

15. Ho YY, Lagares D, Tager AM and Kapoor M. Fibrosis--a lethal component of systemic sclerosis. *Nat Rev Rheumatol*. 2014;10:390-402.

16. Berg EJ and Robinson RJ. Stereoscopic particle image velocimetry analysis of healthy and emphysemic alveolar sac models. *J Biomech Eng*. 2011;133:061004.

17. Borisova E, Lovric G, Miettinen A, Fardin L, Bayat S, Larsson A, Stampanoni M, Schittny JC and Schleputz CM. Micrometer-resolution X-ray tomographic full-volume reconstruction of an intact post-mortem juvenile rat lung. *Histochem Cell Biol*. 2020.

18. Broche L, Perchiazzi G, Porra L, Tannoia A, Pellegrini M, Derosa S, Sindaco A, Batista Borges J, Degrugilliers L, Larsson A, Hedenstierna G, Wexler AS, Bravin A, Verbanck S, Smith BJ, Bates JH and Bayat S. Dynamic Mechanical Interactions Between Neighboring Airspaces Determine Cyclic Opening and Closure in Injured Lung. *Crit Care Med*. 2017;45:687-694.

19. Motta-Ribeiro GC, Hashimoto S, Winkler T, Baron RM, Grogg K, Paula L, Santos A, Zeng C, Hibbert K, Harris RS, Bajwa E and Vidal Melo MF. Deterioration of Regional Lung Strain and Inflammation during Early Lung Injury. *Am J Respir Crit Care Med.* 2018;198:891-902.
20. Perlman CE and Wu Y. In situ determination of alveolar septal strain, stress and effective Young's modulus: an experimental/computational approach. *Am J Physiol Lung Cell Mol Physiol.* 2014;307:L302-10.
21. Rausch SM, Haberthur D, Stampanoni M, Schittny JC and Wall WA. Local strain distribution in real three-dimensional alveolar geometries. *Ann Biomed Eng.* 2011;39:2835-43.
22. Suki B and Parameswaran H. Computational modeling helps uncover mechanisms related to the progression of emphysema. *Drug Discov Today Dis Models.* 2014;70:4245-4249.
23. Geyer H, Caracciolo G, Abe H, Wilansky S, Carerj S, Gentile F, Nesser HJ, Khandheria B, Narula J and Sengupta PP. Assessment of myocardial mechanics using speckle tracking echocardiography: fundamentals and clinical applications. *J Am Soc Echocardiogr.* 2010;23:351-69; quiz 453-5.
24. Mor-Avi V, Lang RM, Badano LP, Belohlavek M, Cardim NM, Derumeaux G, Galderisi M, Marwick T, Nagueh SF, Sengupta PP, Sicari R, Smiseth OA, Smulevitz B, Takeuchi M, Thomas JD, Vannan M, Voigt JU and Zamorano JL. Current and evolving echocardiographic techniques for the quantitative evaluation of cardiac mechanics: ASE/EAE consensus statement on methodology and indications endorsed by the Japanese Society of Echocardiography. *J Am Soc Echocardiogr.* 2011;24:277-313.
25. Perk G, Tunick PA and Kronzon I. Non-Doppler two-dimensional strain imaging by echocardiography--from technical considerations to clinical applications. *J Am Soc Echocardiogr.* 2007;20:234-43.
26. Sareen N and Ananthasubramaniam K. Strain Imaging: From Physiology to Practical Applications in Daily Practice. *Cardiol Rev.* 2016;24:56-69.
27. Jasaityte R, Heyde B and D'Hooze J. Current state of three-dimensional myocardial strain estimation using echocardiography. *J Am Soc Echocardiogr.* 2013;26:15-28.
28. Fischer B, Modersitzki, J. Fast image registration and a new curvature based registration technique. *Linear Algebra and its Applications.* 2004;380:107-124.

29. Vemuri BC, Ye J, Chen Y and Leonard CM. Image registration via level-set motion: applications to atlas-based segmentation. *Med Image Anal.* 2003;7:1-20.
30. Unser PTM. Optimization of mutual information for multiresolution image registration. *IEEE Transactions on Image Processing* 2000;9:2083 - 2099.
31. Stefan Klein JPWP, Marius Staring, Max A Viergever. Adaptive Stochastic Gradient Descent Optimisation for Image Registration. *International Journal of Computer Vision* March 2009;81:227-239.
32. Hawkes DRLISCHDLGHMOLDJ. Nonrigid registration using free-form deformations: application to breast MR images. *IEEE Transactions on Medical Imaging.* 1999;18:712-721.
33. Unser M. Splines: a perfect fit for signal and image processing. *IEEE Signal Processing Magazine* 1999;16:22-38.
34. B.C. Vermuri JY, Y. Chen and C. M. Leonard. A level-set based approach to image registration. *Proc IEEE Workshop MMBIA-2000.* 2000;86-93.
35. Mase GE. *Continuum Mechanics for Engineers*: CRC Press; 2009.
36. Gerard J. Tortora BHD. *Principles of anatomy & physiology.* 15th ed: Willey; 2016.
37. Alicia M. Maceira SKP, Mohammed Khan, Dudley J. Pennell Reference right ventricular systolic and diastolic function normalized to age, gender and body surface area from steady-state free precession cardiovascular magnetic resonance. *European Heart Journal.* 2006;27:2879–2888.
38. *International Assoc. for Bridge and Structural Engineering.*
39. Bresler BaP, K.S.,. *Strength of concrete under combined stresses, ACI Journal*; 1985.
40. Prager. DCDaW. Soil mechanics and plastic analysis or limit design 1952;10:157-165
41. Haddad RA and Akansu AN. A class of fast Gaussian binomial filters for speech and image processing. *IEEE Transactions on Signal Processing.* 1991;39:723-727.
42. Hualiang Zhong JK, and Indrin J. Chetty. Analysis of deformable image registration accuracy using computational modeling. *Medical Physics.* 2010;37:970-979.
43. Audette SSJEBBGTRMA. MRI-Based Medial Axis Extraction and Boundary Segmentation of Cranial Nerves Through Discrete Deformable 3D Contour and Surface

Models. *IEEE Transactions on Medical Imaging*. 2017;36:1711-1721.

44. Piotr Swierczynski BWP, Julia A Schnabel , Colin Macdonald A Level-Set Approach to Joint Image Segmentation and Registration With Application to CT Lung Imaging. *Comput Med Imaging Graph*. 2018;65:58-68.

45. Daegwan Kim NK, Sangmin Lee, Joon Beom Seo. A fast and robust level set motion-assisted deformable registration method for volumetric CT guided lung intervention. *Biocybernetics and Biomedical Engineering*. 2018;38:439-447.

46. Santus P, Pecchiari M, Tursi F, Valenti V, Saad M and Radovanovic D. The Airways' Mechanical Stress in Lung Disease: Implications for COPD Pathophysiology and Treatment Evaluation. *Can Respir J*. 2019;2019.

47. Kononov S, Brewer K, Sakai H, Cavalcante FSA, Sabayanagam CR, Ingenito EP and Suki B. Roles of mechanical forces and collagen failure in the development of elastase-induced emphysema. *American Journal of Respiratory and Critical Care Medicine*. 2001;164:1920-1926.

48. de Ryk J, Thiesse J, Namati E and McLennan G. Stress distribution in a three dimensional, geometric alveolar sac under normal and emphysematous conditions. *Int J Chron Obstruct Pulmon Dis*. 2007;2:81-91.

49. Xu YY, Yamashiro T, Moriya H, Tsubakimoto M, Nagatani Y, Matsuoka S, Murayama S and Grp AS. Strain measurement on four-dimensional dynamic-ventilation CT: quantitative analysis of abnormal respiratory deformation of the lung in COPD. *Int J Chronic Obstr*. 2019;14:65-72.

50. Gerald D. Buckberg NCN, Christopher Nguyen and Mladen J. Kocica What Is the Heart? Anatomy, Function, Pathophysiology, and Misconceptions *J Cardiovasc Dev Dis*. 2018;5:33.

51. Vogelmeier CF, Criner GJ, Martinez FJ, Anzueto A, Barnes PJ, Bourbeau J, Celli BR, Chen R, Decramer M, Fabbri LM, Frith P, Halpin DM, Lopez Varela MV, Nishimura M, Roche N, Rodriguez-Roisin R, Sin DD, Singh D, Stockley R, Vestbo J, Wedzicha JA and Agusti A. Global Strategy for the Diagnosis, Management and Prevention of Chronic Obstructive Lung Disease 2017 Report: GOLD Executive Summary. *Respirology*. 2017;22:575-601.

52. Rabe KF, Hurd S, Anzueto A, Barnes PJ, Buist SA, Calverley P, Fukuchi Y, Jenkins

C, Rodriguez-Roisin R, van Weel C, Zielinski J and Global Initiative for Chronic Obstructive Lung D. Global strategy for the diagnosis, management, and prevention of chronic obstructive pulmonary disease: GOLD executive summary. *Am J Respir Crit Care Med.* 2007;176:532-55.

53. Labaki WW, Martinez CH, Martinez FJ, Galban CJ, Ross BD, Washko GR, Barr RG, Regan EA, Coxson HO, Hoffman EA, Newell JD, Jr., Curran-Everett D, Hogg JC, Crapo JD, Lynch DA, Kazerooni EA and Han MK. The Role of Chest Computed Tomography in the Evaluation and Management of the Patient with Chronic Obstructive Pulmonary Disease. *Am J Respir Crit Care Med.* 2017;196:1372-1379.

54. Celli BR, Cote CG, Marin JM, Casanova C, Montes de Oca M, Mendez RA, Pinto Plata V and Cabral HJ. The body-mass index, airflow obstruction, dyspnea, and exercise capacity index in chronic obstructive pulmonary disease. *N Engl J Med.* 2004;350:1005-12.

55. Martinez FJ, Foster G, Curtis JL, Criner G, Weinmann G, Fishman A, DeCamp MM, Benditt J, Sciruba F, Make B, Mohsenifar Z, Diaz P, Hoffman E, Wise R and Group NR. Predictors of mortality in patients with emphysema and severe airflow obstruction. *Am J Respir Crit Care Med.* 2006;173:1326-34.

56. Haruna A, Muro S, Nakano Y, Ohara T, Hoshino Y, Ogawa E, Hirai T, Niimi A, Nishimura K, Chin K and Mishima M. CT scan findings of emphysema predict mortality in COPD. *Chest.* 2010;138:635-40.

57. Kirby M, Tanabe N, Tan WC, Zhou G, Obeidat M, Hague CJ, Leipsic J, Bourbeau J, Sin DD, Hogg JC, Coxson HO, Can CCRG, Canadian Respiratory Research N and CanCold Collaborative Research Group tCRRN. Total Airway Count on Computed Tomography and the Risk of Chronic Obstructive Pulmonary Disease Progression. Findings from a Population-based Study. *Am J Respir Crit Care Med.* 2018;197:56-65.

58. Park TS, Lee JS, Seo JB, Hong Y, Yoo JW, Kang BJ, Lee SW, Oh YM, Lee SD and Group KS. Study Design and Outcomes of Korean Obstructive Lung Disease (KOLD) Cohort Study. *Tuberc Respir Dis (Seoul).* 2014;76:169-74.

59. Jung Keun Choi DP, Jeoung Oh Lee. Normal Predictive Values of Spirometry in Korean Population. *Tuberculosis and Respiratory Diseases.* 2005;58:230-242.

60. Feng Y, Wang J, Zhang Y and Wang S. One-Lung Ventilation with Additional

Ipsilateral Ventilation of Low Tidal Volume and High Frequency in Lung Lobectomy. *Med Sci Monit.* 2016;22:1589-92.

61. Terry M. Therneau PMG. *Modeling Survival Data: Extending the Cox Model*: Springer, New York. ; 2000.

62. Alboukadel Kassambara MKaPB. *survminer: Drawing Survival Curves using 'ggplot2'*; 2019.

63. Wickham H. *ggplot2: Elegant Graphics for Data Analysis*: Springer-Verlag New York; 2016.

64. Martinez FJ, Han MK, Allinson JP, Barr RG, Boucher RC, Calverley PMA, Celli BR, Christenson SA, Crystal RG, Fageradegras M, Freeman CM, Groenke L, Hoffman EA, Kesimer M, Kostikas K, Paine R, Rafii S, Rennard SI, Segal LN, Shaykhiev R, Stevenson C, Tal-Singer R, Vestbo J, Woodruff PG, Curtis JL and Wedzicha JA. At the Root: Defining and Halting Progression of Early Chronic Obstructive Pulmonary Disease. *American Journal of Respiratory and Critical Care Medicine.* 2018;197:1540-1551.

65. Agusti A and Faner R. The Changing Landscape of Chronic Obstructive Pulmonary Disease. *Am J Respir Crit Care Med.* 2018;198:978-981.

66. Walker PP, Pompilio PP, Zanaboni P, Bergmo TS, Prikk K, Malinovschi A, Montserrat JM, Middlemass J, Sonc S, Munaro G, Marusic D, Sepper R, Rosso R, Siriwardena AN, Janson C, Farre R, Calverley PMA and Dellaca RL. Telemonitoring in Chronic Obstructive Pulmonary Disease (CHROMED). A Randomized Clinical Trial. *Am J Respir Crit Care Med.* 2018;198:620-628.

67. Ekstrom M, Bornefalk-Hermansson A, Wysham N, Currow DC and MacIntyre N. Spirometric Volumes and Breathlessness Across Levels of Airflow Limitation: The COPDGene Study. *Am J Respir Crit Care Med.* 2018.

68. Lusk CM, Wenzlaff AS, Watza D, Sieren JC, Robinette N, Walworth G, Petrich M, Neslund-Dudas C, Flynn MJ, Song T, Spizarny D, Simoff MJ, Soubani AO, Gadgeel S and Schwartz AG. Quantitative Imaging Markers of Lung Function in a Smoking Population Distinguish COPD Subgroups with Differential Lung Cancer Risk. *Cancer Epidemiol Biomarkers Prev.* 2019;28:724-730.

69. Tobon-Trujillo M, Gil-Torres P, Torres-Gonzalez J, Canas Arboleda A and Celis-

Preciado C. Smokers with Normal Spirometry: Impact of Computed Tomography-detected Emphysema, Functional Mechanisms of Dyspnea, and Clinical Significance of Symptoms. *Am J Respir Crit Care Med.* 2018;198:1085-1087.

70. Wan ES, Fortis S, Regan EA, Hokanson J, Han MK, Casaburi R, Make BJ, Crapo JD, DeMeo DL, Silverman EK and Investigators CO. Longitudinal Phenotypes and Mortality in Preserved Ratio Impaired Spirometry in the COPD Gene Study. *Am J Respir Crit Care Med.* 2018;198:1397-1405.

71. Miravittles M. What We Talk about When We Talk about Exacerbations of Chronic Obstructive Pulmonary Disease. *Am J Respir Crit Care Med.* 2019;199:2-4.

72. Bodduluri S, Reinhardt JM, Hoffman EA, Newell JD, Jr., Nath H, Dransfield MT, Bhatt SP and Investigators CO. Signs of Gas Trapping in Normal Lung Density Regions in Smokers. *Am J Respir Crit Care Med.* 2017;196:1404-1410.

73. Gonzalez G, Ash SY, Vegas-Sanchez-Ferrero G, Onieva Onieva J, Rahaghi FN, Ross JC, Diaz A, San Jose Estepar R, Washko GR, CopdGene and Investigators E. Disease Staging and Prognosis in Smokers Using Deep Learning in Chest Computed Tomography. *Am J Respir Crit Care Med.* 2018;197:193-203.

74. Raghu G, Collard HR, Egan JJ, Martinez FJ, Behr J, Brown KK, Colby TV, Cordier JF, Flaherty KR, Lasky JA, Lynch DA, Ryu JH, Swigris JJ, Wells AU, Ancochea J, Bouros D, Carvalho C, Costabel U, Ebina M, Hansell DM, Johkoh T, Kim DS, King TE, Jr., Kondoh Y, Myers J, Muller NL, Nicholson AG, Richeldi L, Selman M, Dudden RF, Griss BS, Protzko SL, Schunemann HJ and Fibrosis AEJACoIP. An official ATS/ERS/JRS/ALAT statement: idiopathic pulmonary fibrosis: evidence-based guidelines for diagnosis and management. *Am J Respir Crit Care Med.* 2011;183:788-824.

75. Olson AL and Swigris JJ. Idiopathic pulmonary fibrosis: diagnosis and epidemiology. *Clin Chest Med.* 2012;33:41-50.

76. Adegunsoye A, Oldham JM, Bellam SK, Montner S, Churpek MM, Noth I, Vij R, Streck ME and Chung JH. Computed Tomography Honeycombing Identifies a Progressive Fibrotic Phenotype with Increased Mortality across Diverse Interstitial Lung Diseases. *Ann Am Thorac Soc.* 2019;16:580-588.

77. Jacob J, Bartholmai BJ, Rajagopalan S, van Moorsel CHM, van Es HW, van Beek

FT, Struik MHL, Kokosi M, Egashira R, Brun AL, Nair A, Walsh SLF, Cross G, Barnett J, de Lauretis A, Judge EP, Desai S, Karwoski R, Ourselin S, Renzoni E, Maher TM, Altmann A and Wells AU. Predicting Outcomes in Idiopathic Pulmonary Fibrosis Using Automated Computed Tomographic Analysis. *Am J Respir Crit Care Med.* 2018;198:767-776.

78. Montesi SB, Fisher JH, Martinez FJ, Selman M, Pardo A and Johannson KA. Update in Interstitial Lung Disease 2019. *Am J Respir Crit Care Med.* 2020.

79. Wu X, Kim GH, Salisbury ML, Barber D, Bartholmai BJ, Brown KK, Conoscenti CS, De Backer J, Flaherty KR, Gruden JF, Hoffman EA, Humphries SM, Jacob J, Maher TM, Raghu G, Richeldi L, Ross BD, Schlenker-Herceg R, Sverzellati N, Wells AU, Martinez FJ, Lynch DA, Goldin J and Walsh SLF. Computed Tomographic Biomarkers in Idiopathic Pulmonary Fibrosis. The Future of Quantitative Analysis. *Am J Respir Crit Care Med.* 2019;199:12-21.

80. Fukihara J, Kondoh Y, Brown KK, Kimura T, Kataoka K, Matsuda T, Yamano Y, Suzuki A, Furukawa T, Sumikawa H, Takahashi O, Johkoh T, Tanaka T, Fukuoka J, Hashimoto N and Hasegawa Y. Probable usual interstitial pneumonia pattern on chest CT: is it sufficient for a diagnosis of idiopathic pulmonary fibrosis? *Eur Respir J.* 2020;55.

81. Behr J. A small change in FVC but a big change for IPF: defining the minimal clinically important difference. *Am J Respir Crit Care Med.* 2011;184:1329-30.

82. Collard HR, King TE, Jr., Bartelson BB, Vourlekis JS, Schwarz MI and Brown KK. Changes in clinical and physiologic variables predict survival in idiopathic pulmonary fibrosis. *Am J Respir Crit Care Med.* 2003;168:538-42.

83. Jegal Y, Kim DS, Shim TS, Lim CM, Do Lee S, Koh Y, Kim WS, Kim WD, Lee JS, Travis WD, Kitaichi M and Colby TV. Physiology is a stronger predictor of survival than pathology in fibrotic interstitial pneumonia. *Am J Respir Crit Care Med.* 2005;171:639-44.

84. Sahmin Lee, Seunghyun Choi, Sehwon Kim, Yeongjin Jeong, Kyusup Lee, Seung-Ho Hur, Sun Ro Lee, Eun-Jeong Lee, Min-Jung Sin, Namkug Kim, Jong-Min Song Validation of Three-Dimensional Echocardiographic Principal Strain Analysis for Assessing Left Ventricular Contractility: An Animal Study *Medical Physics.* 2019;46:2137-2144.

85. Ruta Jasaityte BH, Jan D'hooge. Current State of Three-Dimensional Myocardial

- Strain Estimation Using Echocardiography. *J Am Soc Echocardiogr.* 2013;26:15-28.
86. Gianni Pedrizzetti P, Shantanu Sengupta, MD, Giuseppe Caracciolo, MD, Chan Seok Park, MD, PhD, Makoto Amaki, MD, PhD, Georg Goliash, MD, PhD, Jagat Narula, MD, PhD, Partho P. Sengupta, MD. Three-Dimensional Principal Strain Analysis for Characterizing Subclinical Changes in Left Ventricular Function. *Journal of American Society of Echocardiology.* 2014;27:1041-1050.
87. Alessandro Satriano BH, Mariam Narous , Derek V Exner , Yoko Mikami , Monica M Attwood , John V Tyberg , Carmen P Lydell , Andrew G Howarth , Nowell M Fine , James A White Clinical Feasibility and Validation of 3D Principal Strain Analysis From Cine MRI: Comparison to 2D Strain by MRI and 3D Speckle Tracking Echocardiography *Int J Cardiovasc Imaging.* 2017;33:1979-1992.
88. Nima Milani-Nejad PMLJ. Small and Large Animal Models in Cardiac Contraction Research: Advantages and Disadvantages 2014;141:235-249.
89. Fredrik Orderud SIR. Real-time 3D segmentation of the left ventricle using deformable subdivision surfaces. Paper presented at: 2008 IEEE Conference on Computer Vision and Pattern Recognition; 2008; Anchorage, AK, USA
90. Mangual JO, De Luca A, Toncelli L, Domenichini F, Galanti G and Pedrizzetti G. Three-dimensional reconstruction of the functional strain-line pattern in the left ventricle from 3-dimensional echocardiography. *Circ Cardiovasc Imaging.* 2012;5:808-9.
91. Pedrizzetti G, Sengupta S, Caracciolo G, Park CS, Amaki M, Goliash G, Narula J and Sengupta PP. Three-dimensional principal strain analysis for characterizing subclinical changes in left ventricular function. *J Am Soc Echocardiogr.* 2014;27:1041-1050 e1.
92. Evangelista A, Gabriele S, Nardinocchi P, Piras P, Puddu PE, Teresi L, Torromeo C and Varano V. Non-invasive assessment of functional strain lines in the real human left ventricle via speckle tracking echocardiography. *J Biomech.* 2015;48:465-71.
93. Reddy JN. *An Introduction to Continuum Mechanics.* 2nd ed: Cambridge University Press; 2013.
94. Gurney JW. Pathophysiology of obstructive airways disease. *Radiol Clin North Am.* 1998;36:15-27.
95. Miller MR, Quanjor, P. H., Swanney, M. P., Ruppel, G. & Enright, P. L. Interpreting

lung function data using 80% predicted and fixed thresholds misclassifies more than 20% of patients. *Chest*. 2011;139:52-59.

96. Gardner ZS, Ruppel, G. L. & Kaminsky, D. A. . Grading the severity of obstruction in mixed obstructive-restrictive lung disease. . *Chest*. 2011;140:598–603

97. Charlene S. Stahr CRS, Martin Donnelley, Nigel Farrow, Kaye S. Morgan, Graeme Zosky, Richard C. Boucher, Karen K. W. Siu, Marcus A. Mall, David W. Parsons, Stephen Dubsy & Andreas Fouras Quantification of heterogeneity in lung disease with image-based pulmonary function testing. *Scientific Rports*. 2016;6:29438.

98. Pahal P, Hashmi MF, Sharma S. Chronic Obstructive Pulmonary Disease (COPD) Compensatory Measure. In: *StatPearls*. Treasure Island (FL): StatPearls Publishing; 2020.

감사의 글

저는 앞에서 이끌어주시고, 옆에서 함께하신 많은 분들의 지원과 가르침이 있어 학위를 완료하였습니다.

본 학위논문의 연구주제 안에 과가 있다면 온전히 저의 잘못이며, 공이 있다면 그 절반은 도움주신 모든 분들의 덕입니다.

중개임상연구에 갓 진입한 공학인의 적응을 여러 의료진께서 기다리고 이끌어주셨습니다. 임상적으로 무엇이 중요하고 무엇이 필요한지를 공학인을 이해하면서 가교하고 계몽해 주신 서준범 교수님을 필두로, 오연목 교수님, 이호연 교수님, 이상민 A 교수님, 이상민 B 교수님, 송종민 교수님, 이사민 교수님 모두 고개숙여 감사 올립니다.

그리고 산업계에서 일하던 저를 중개임상연구로 이끌어주신 지도교수님, 김남국 교수님께 감사 드립니다. 연구 내용 뿐만이 아니라, 공학자가 의료연구에 뿌리내려 독립된 연구자가 되기 위해 갖춰야 할 것들을 말로도, 그리고 본인께서 행동하는 예시로서도 보여주셨습니다.

- 관습적 차이를 때로는 인정하고 때로는 극복하면서 좋은 의도가 살아나게 하는 방법,
- 연구자로서 자생력을 가지기 위한 연구와 협력의 기초,
- 불확실, 불완전한 상황에서 먼저 움직이고 제시하면서 일을 만들어나가는 적극성,
- 좋지 않은 결과에도 굴하지 않고 계속 시도하면서 결과를 만들어나가는 기저 의지,
- 좋은 성과와 명성에도 권위보다 논리를 앞세우는 진솔함 등

감히 배웠다고 할 만큼 제 삶에 체현시키지는 못하였으나, 곱씹을 수 있을만큼 마음에 담았습니다.

의료영상의 정합과 여러 처리기법들을 가르쳐 주신 이준구 교수님께도 감사드립니다. 교수님께서서는 너털웃음과 유머로 격려를 하시면서도, 동시에 놓치고 있는 중요한 포인트가 보

일 때 마다 짚어 주셨습니다. 부드럽지만 정확했던 많은 지적과 조언들에 감사드립니다.

학교 동문으로 연구실에 계신 동안에는 가까이서 여러 조언을 해 주시고, 결국 심사위원으로 참여해 주신 하호진 교수님께도 감사 올립니다.

제가 겪었던 중개임상연구의 구조 안에서, 언제나 중심이 되는 것은 의료영상이었습니다. 의료영상의 관리, 운용, 분할 등을 신속 정확한 처리와 함께 넉넉한 웃음으로 지원해 주신 박희준 선생님께 깊이 감사 드립니다. 같은 맥락으로 김지은 선생님과 고지연 선생님께도 감사드립니다.

연구실 선배로서 낯선 이를 선뜻 받아주시고 적응을 도와주신 정준호 박사님, 이민호 박사님, 장택진 선생님께도 깊이 감사드립니다. 먼저 가 보신 길 앞에 어떤 이슈들이 있었는지 허심탄회하게 말씀주신 요소들이, 비슷한 길을 지나오면서 이정표가 되었습니다.

연구실의 동료로서 실무에서 협력과 지원을 주고받았던 함성원 선생님, 권진희 선생님, 권재영 선생님께도 감사드립니다. 제가 더 해드리지 못한 부분에 대한 미안함과, 제가 더 배우지 못한 부분에 대한 아쉬움이 남습니다.

서로의 연구 내용에 대한 과감한 수학적/물리적 토의를 함께 해 주신 정계삼 선생님, 김세환 선생님께도 감사 드립니다. 연구의 성과로 이어진 것이 아니라도, 두 분과 나눈 토의들로 인해 서로가 깊이와 넓이 면에서 매우 효과적인 확장을 이루었다고 생각합니다.

전부 마무리하지 못한 연구를 같은 연구실의 이한 선생님, 황정은 박사님께 이관하였습니다. 참여 결정에 이어 보여주시는 열띤 토의와 판단들에 감사 드립니다. 불러 주시면 언제라도 기존 상황을 설명드리고 토의에 참여하겠습니다.

저는 학위의 수료에 즈음하여 환자맞춤형 수술지원 솔루션을 만드는 의료 벤처 창업에 참여 하였습니다. 당시 연구실 3D 프린팅 팀으로서 함께하시던 이상욱 선생님, 김태훈 선생님, 김명준 선생님, 송현경 선생님, 장유정 선생님, 권은서 선생님, 홍다영 선생님 등 여러 분들께서 본인들의 경험과 판단을 아낌없이 나눠 주셨고, 이 중 몇 선생님들께서는 회사로 자리를 옮겨 지금도 함께 일하고 있습니다. 이 자리를 빌어 다시 한번 감사 드립니다.

그리고 지금은 대표로 모시고 있는 김국배 박사님께서 연구실에 온 첫 날부터 지금까지

여러가지 조언을 주셨습니다. 회사 일을 함께하면서 가끔은 눈에 안 보이게 서로를 돕고 가끔은 생각이 달라 줄다리기도 하지만, 결과적으로 제가 중개임상연구에 들어온 이후 가장 오랫동안 함께 일하며 교류하고 있습니다. 그동안 주신 여러 배려와 조언에 재차 감사 드립니다.

부족한 제 기억으로 인해, 미처 적지 못한 분들 중에서도 함께하면서 배우고 또 지원을 받은 많은 분들이 계실 것입니다. 감사 드리며, 너그러운 이해를 구합니다.

미욱한 자식이 공학을 한다 하여, 우려 속에서도 자식의 선택을 믿어주신 부모님께 깊이 감사 드립니다. 제가 있는 자리에서도 가훈처럼 앞장서 맞서고 동행을 섬기며 나라에 보탬이 되겠습니다.

마지막으로, 제 평생의 도반으로서 학문적 화두를 함께하고 있는 아내에게 한량없는 빛을 졌습니다. 당신은 저와 가장 가까이에서 가장 많은 이야기를 나눠주셨고, 제 삶에 이어 제 연구에도 빛이 되어 주셨습니다.

곧 같이 한 날이 같이 하지 않은 날보다 많아집니다.

다시 태어나도 당신을 만나서 사랑을 하고 함께 연구하겠습니다.